



NAVAL POSTGRADUATE SCHOOL

MONTEREY, CALIFORNIA

THESIS

**INVESTIGATION OF 2-DIMENSIONAL ISOTROPY OF
UNDER-ICE ROUGHNESS IN THE BEAUFORT GYRE
AND IMPLICATIONS FOR MIXED LAYER OCEAN
TURBULENCE**

by

Timothy P. McGeehan

March 2008

Thesis Advisor:
Second Reader:

Timothy P. Stanton
William J. Shaw

Approved for public release; distribution is unlimited

THIS PAGE INTENTIONALLY LEFT BLANK

REPORT DOCUMENTATION PAGE			<i>Form Approved OMB No. 0704-0188</i>	
Public reporting burden for this collection of information is estimated to average 1 hour per response, including the time for reviewing instruction, searching existing data sources, gathering and maintaining the data needed, and completing and reviewing the collection of information. Send comments regarding this burden estimate or any other aspect of this collection of information, including suggestions for reducing this burden, to Washington headquarters Services, Directorate for Information Operations and Reports, 1215 Jefferson Davis Highway, Suite 1204, Arlington, VA 22202-4302, and to the Office of Management and Budget, Paperwork Reduction Project (0704-0188) Washington DC 20503.				
1. AGENCY USE ONLY (Leave blank)		2. REPORT DATE March 2008	3. REPORT TYPE AND DATES COVERED Master's Thesis	
4. TITLE AND SUBTITLE Investigation of 2-Dimensional Under-ice Roughness in the Beaufort Gyre and Implications for Mixed Layer Ocean Turbulence			5. FUNDING NUMBERS N/A	
6. AUTHOR(S) Timothy P. McGeehan				
7. PERFORMING ORGANIZATION NAME(S) AND ADDRESS(ES) Naval Postgraduate School Monterey, CA 93943-5000			8. PERFORMING ORGANIZATION REPORT NUMBER N/A	
9. SPONSORING /MONITORING AGENCY NAME(S) AND ADDRESS(ES) N/A			10. SPONSORING/MONITORING AGENCY REPORT NUMBER N/A	
11. SUPPLEMENTARY NOTES The views expressed in this thesis are those of the author and do not reflect the official policy or position of the Department of Defense or the U.S. Government.				
12a. DISTRIBUTION / AVAILABILITY STATEMENT Approved for public release; distribution is unlimited			12b. DISTRIBUTION CODE UU	
13. ABSTRACT (maximum 200 words) <p>The two-dimensional (2D) spectral properties, including the degree of isotropy, of under-ice roughness in the Beaufort Gyre were investigated. Under-ice roughness plays an important role in turbulent ocean heat, salt, and momentum fluxes that determine the delicate balance between surface forcing and the ocean interior that sustains or reduces the perennial ice cover. Accurate characterization of this roughness is important for numerical modeling and prediction of the Arctic air-ice-ocean system, which will play a significant role as the US Navy increases its strategic presence in the ice-diminished Arctic Ocean. Ice draft data from moored upward looking echosounders of the Beaufort Gyre Exploration Project and ice motion derived from trajectories of International Arctic Buoy Program buoys were combined to create directional sections of ice draft. Autocorrelation functions were created for each segment which were then combined to make a 2D autocorrelation function. The 2D FFT was taken of this in order to yield a 2D spectrum, from which isotropy and other spectral properties could be determined. The processing routine was tested on several synthetic test datasets and in each case produced the correct output. Two years of data from three moorings in the Beaufort all provided 2D spectra which showed weak anisotropy of the under-ice roughness. Error estimates were determined by Monte Carlo simulations. For each dataset, most of the variance of the underside morphology was contained in a wavenumber band between 0.001 and 0.01m^{-1} (100-1000m). There were no distinct, preferred wavelengths. Spectral levels ranged from $1.2 - 4.2 \times 10^4 \text{ m}^2$ for Mooring C (2004-2005) to $0.2 - 1.6 \times 10^4 \text{ m}^2$ for Mooring A (2004-2005).</p>				
14. SUBJECT TERMS isotropy, sea ice, pressure ridges, ice keels, ice roughness, Beaufort Gyre, Arctic Ocean			15. NUMBER OF PAGES 73	
			16. PRICE CODE	
17. SECURITY CLASSIFICATION OF REPORT Unclassified	18. SECURITY CLASSIFICATION OF THIS PAGE Unclassified	19. SECURITY CLASSIFICATION OF ABSTRACT Unclassified	20. LIMITATION OF ABSTRACT UU	

THIS PAGE INTENTIONALLY LEFT BLANK

Approved for public release; distribution is unlimited

**INVESTIGATION OF 2-DIMENSIONAL ISOTROPY OF UNDER-ICE
ROUGHNESS IN THE BEAUFORT GYRE AND IMPLICATIONS FOR MIXED
LAYER OCEAN TURBULENCE**

Timothy P. McGeehan
Lieutenant, United States Navy
B.S., United States Naval Academy, 2000

Submitted in partial fulfillment of the
requirements for the degree of

**MASTER OF SCIENCE IN METEOROLOGY AND PHYSICAL
OCEANOGRAPHY**

from the

**NAVAL POSTGRADUATE SCHOOL
March 2008**

Author: Timothy P. McGeehan

Approved by: Timothy P. Stanton
Thesis Advisor

William J. Shaw
Second Reader

Mary L. Batteen
Chairman, Department of Oceanography

THIS PAGE INTENTIONALLY LEFT BLANK

ABSTRACT

The two-dimensional (2D) spectral properties, including the degree of isotropy, of under-ice roughness in the Beaufort Gyre were investigated. Under-ice roughness plays an important role in turbulent ocean heat, salt, and momentum fluxes that determine the delicate balance between surface forcing and the ocean interior that sustains or reduces the perennial ice cover. Accurate characterization of this roughness is important for numerical modeling and prediction of the Arctic air-ice-ocean system, which will play a significant role as the US Navy increases its strategic presence in the ice-diminished Arctic Ocean. Ice draft data from moored upward looking echosounders of the Beaufort Gyre Exploration Project and ice motion derived from trajectories of International Arctic Buoy Program buoys were combined to create directional sections of ice draft. Autocorrelation functions were created for each segment which were then combined to make a 2D autocorrelation function. The 2D FFT was taken of this in order to yield a 2D spectrum, from which isotropy and other spectral properties could be determined. The processing routine was tested on several synthetic test datasets and in each case produced the correct output. Two years of data from three moorings in the Beaufort all provided 2D spectra which showed weak anisotropy of the under-ice roughness. Error estimates were determined by Monte Carlo simulations. For each dataset, most of the variance of the underside morphology was contained in a wavenumber band between 0.001 and 0.01m^{-1} (100-1000m). There were no distinct, preferred wavelengths. Spectral levels ranged from $1.2 - 4.2 \times 10^4 \text{ m}^2$ for Mooring C (2004-2005) to $0.2 - 1.6 \times 10^4 \text{ m}^2$ for Mooring A (2004-2005).

THIS PAGE INTENTIONALLY LEFT BLANK

TABLE OF CONTENTS

I.	INTRODUCTION.....	1
A.	CURRENT EVENTS.....	1
B.	UNDER ICE ROUGHNESS FEATURES AND DEFINITIONS.....	2
C.	SIGNIFICANCE	3
D.	STUDY OBJECTIVES.....	5
II.	DATA SELECTION.....	7
A.	ICE DRAFT DETERMINATION.....	7
1.	Submarine Data	8
2.	Mooring Data	10
B.	CONVERTING TO A SPATIAL SERIES OF ICE DRAFT	11
C.	ICE MOTION DETERMINATION	11
III.	DATA PROCESSING	13
A.	ICE DRAFT DATA PROCESSING	13
B.	ICE MOTION DATA PROCESSING	19
C.	COMBINING THE ICE DRAFT AND MOTION DATA.....	24
IV.	ANALYSIS AND DISCUSSION	31
A.	TEST CASES	31
1.	Single Sine Wave	31
2.	Single Sine Wave Derived from Different Motion Data.....	33
3.	2 Sine Waves of Different Wavelengths but Different Amps and Different Orientation.....	35
4.	Single Sinc Function	37
B.	BEAUFORT GYRE DATA	39
1.	Mooring C: August 2004–August 2005	39
2.	Summary for Other Data Sets	45
C.	SPATIAL AND TEMPORAL COMPARISONS	46
D.	COMPARISONS TO OTHER RESEARCHERS	49
E.	TURBULENCE IMPLICATIONS.....	50
F.	POSSIBLE MITIGATING EFFECT	51
V.	CONCLUSIONS	53
	LIST OF REFERENCES	55
	INITIAL DISTRIBUTION LIST	59

THIS PAGE INTENTIONALLY LEFT BLANK

LIST OF FIGURES

Figure 1.	Simplified Arctic sound speed profiles. Model 1 is based on a sequence of plane parallel layers each with a constant gradient whereas Model 2 is based on a series of flat layers of constant velocity and density (Kutschale, 1969).	4
Figure 2.	Acoustic ray paths for a source at 100m depth using Model 1 from Fig. 1 (Kutschale, 1969).	5
Figure 3.	Surveyed ice ridge from APLIS 2007 and an extrapolated ice keel using the standard ratio for ice keel draft to ridge height of 3.2:1.	8
Figure 4.	Original “Gore Box” and current release data for some submarine collected upward looking sonar ice draft data (National Snow and Ice Data Center, 2006).	9
Figure 5.	Crewmembers inspect sail damage on USS SARGO (SSN-583) after colliding with an ice keel in the Bering Sea in February 1960 (Nicholson, 2008).	10
Figure 6.	BGEP Mooring Locations.	13
Figure 7.	Schematic of ULS mooring (Krishfield and Proshutinsky, 2006).	14
Figure 8.	Effect of echosounder beam width on apparent keel profile. Note that the apparent width and average draft increase (Wadhams, 1978).	15
Figure 9.	(a) View from below ice keel showing sampling directions perpendicular to the keel and cutting across it at 75° . (b) Apparent keel profiles as a function of sampling angle. $\theta = 0^\circ$ and $\theta = 90^\circ$ correspond to sampling directions perpendicular and parallel to the keel axis, respectively. Note that the apparent width and average draft increase as the angle becomes greater.	17
Figure 10.	(a) View from below field of keels with sampling directions 0 and 75° . (b) Apparent draft profiles from field of regularly spaced keels as a function of sampling angle. Note the increase in apparent spacing of the ice keels as the angle increases.	18
Figure 11.	Drift tracks of all buoys in mooring area from 2003-2005.	20
Figure 12.	Tracks of all IABP buoys passing within 250km of mooring C from 2003-2005.	22
Figure 13.	Example time series of motion compiled at Mooring C: August 2004-August 2005.	23
Figure 14.	Ice draft time series, distance series, and autocorrelation function for Segment #50 at Mooring C.	25
Figure 15.	Combined autocorrelation spatial coverage.	26
Figure 16.	Cumulative distribution functions of ice keel spacing. Plot (a) is derived from narrow beam sonar in the Beaufort Sea: open circles have a threshold of 0m and closed circles have a threshold of 3m. Plot (b) is derived from wide beam sonar in the Eurasian Basin: open circles have a threshold of 0m and closed circles have a threshold of 15m (after Wadhams and Davy, 1986).	29

Figure 17.	(a) Field generated from single sinusoid. (b) Resulting 2D spectrum with energy peaks at correct wavenumbers. (c) Spectral cross section with vertical axis scaled by wavenumber. Note peak energy at correct wave number.	32
Figure 18.	2D autocorrelation plot for field created from a single sinusoid. Note the distortion caused by the angular binning process as angles come less perpendicular to the axis of the crests.	33
Figure 19.	(a) Field generated from sinusoid. (b) 2D spectrum from field sampled with different ice motion data. (c) Spectral cross section.	34
Figure 20.	Sinusoids #1 and #2 which combine to make up the composite field of two sinusoids with differing amplitude, wavelength, and orientation.	35
Figure 21.	(a) Composite field from two sinusoids. (b) 2D spectrum of field. (c) Spectral cross sections with peak energy and relative amplitude correctly represented.	36
Figure 22.	(a) Field from single sinc function. (b) 2D spectrum from field. (c) Spectral cross section; note the decreasing harmonics at higher wavenumbers.	38
Figure 23.	Mooring C: 2004-2005. (a) 2D spectrum. (b) 8 energy conserving spectral cross sections (000 to 157.5° each 22.5°). (c) 8 spectral cross sections.	40
Figure 24.	(a) 2 radial slices through 2D spectrum. (b) 1 sigma confidence intervals for each slice. The red lines represent the + and - 1 sigma confidence intervals for the spectral slice taken along the red dotted line in (a) and the green lines are the confidence intervals for the slice taken along the green dotted line. (c) 2 sigma confidence intervals.	43
Figure 25.	(a) 2 radial slices through 2D spectrum. (b) 1 sigma confidence limits for each slice. The red lines represent the + and - 1 sigma confidence intervals for the spectral slice taken along the red dotted line in (a) and the green lines are the confidence intervals for the slice taken along the green dotted line. (c) 2 sigma confidence intervals.	44
Figure 26.	1 sigma confidence intervals from the spectral cross sections from the synthetic “red” field taken in the same directions as Fig. 25.	45
Figure 27.	2D spectra of under ice roughness from August 2003-August 2004. (a) Mooring A. (b) Mooring B. (c) Mooring C.	47
Figure 28.	2D spectra of under ice roughness from August 2004-August 2005. (a) Mooring A. (b) Mooring B. (c) Mooring C.	48
Figure 29.	Ridge orientation vectors (Davis and Wadhams, 1995).	49
Figure 30.	Density profiles from APLIS 2007. Note the shallow pycnocline; historically the pycnocline has been observed near 35m.	51
Figure 31.	Plot of APLIS 2007 ice floe rotation (Hutchings, 2007).	52

ACKNOWLEDGMENTS

There were a number of people who made this project and associated research possible. I'd like to thank:

At the Naval Postgraduate School: Research Associate Professor Tim Stanton, Research Assistant Professor Bill Shaw, Jim Stockel, Rob Wyland, and CDR Denise Kruse.

At International Arctic Buoy Program: Ignatius Rigor and Mark Ortmeyer.

At Submarine Development Squadron FIVE Detachment Arctic Submarine Laboratory: CAPT Ed Hasel, Jeff Gossett, and Barry Campbell.

At the University of Washington Applied Physics Laboratory: Fred Karig and Tim Wen.

The National Science Foundation.

Most importantly, at home: my wife Kristi and son Aidan.

THIS PAGE INTENTIONALLY LEFT BLANK

I. INTRODUCTION

A. CURRENT EVENTS

Recent changes in the Arctic Ocean and specifically its diminishing ice cover have received significant attention both in scientific circles and amongst the general public. The current International Polar Year is bringing increased awareness and gathering crucial data needed to understand these changes. An ice-diminished Arctic is also of strategic significance to the national security of the United States. The viability of both the Northern Sea Route and the Northwest Passage as navigable shipping lanes for the first time in recorded history combined with the new feasibility of resource exploitation (minerals, oil, fisheries) in the Arctic Basin itself has led many nations to reassert or even stake new claims in the region. Russia, Norway, Sweden, Finland, Denmark, Iceland, Canada and the United States all have major interests in the Arctic and each seeks to extend their Exclusive Economic Zone (EEZ) in any way possible. A 130 year long dispute continues between the United States and Russia over the location of a line dividing possession of the Bering Sea between Siberia and Alaska (Damron, 1997). Norway and Russia have competing claims to fishing rights in the Barents Sea (BBC News, 2005). Canada insists that the Northwest Passage lies within Canadian territorial waters and that they will assert sovereign control of it whereas the United States and many other countries claim international rights to use it for shipping (Shukman, 2007). Most recently, in the summer of 2007, the Russian Federation submitted a formal claim for over 45% of the Arctic seafloor, including the North Pole itself.

The summer of 2007 also saw several military developments. A Russian submersible symbolically planted a flag on the ocean floor at the geographic North Pole. Canada announced that it would enhance its military presence in the Arctic, including building two new military facilities; one for cold-weather warfare training at Resolute Bay and the other a deep-water port on the northern end of Baffin Island (Reid, 2007). The Canadian government also placed an order for six to eight new Polar Class 5 Arctic Offshore Patrol Ships. The vessels will be armed and according to Prime Minister

Harper, they will “allow us patrol the Arctic waters in the Northwest Passage when it matters (CBC News, 2007).” An American guided missile cruiser, USS NORMANDY (CG 60), conducted a patrol across the Arctic Circle north of Iceland to show that the US Navy maintains the capability to operate in the far north. USCGC HEALY conducted a bathymetric survey of the Chukchi Cap in coordination with NOAA’s Office of Coast Survey “to better understand its morphology and the potential for including this area within the United States’ extended continental shelf under the United Nations Convention on Law of the Sea (Elliott, 2007).” In this “gold rush” atmosphere, there is developing potential for armed conflict over both resources and access. At the very least, the US Navy can be expected to conduct routine Freedom of Navigation demonstrations, sending ships to physically challenge territorial claims that the US does not recognize.

In order to safely operate in the Arctic, whether a vessel is military, merchant, or a tourist cruise ship, ice modeling and the resulting forecasting will become as important as routine weather forecasting is today. There are a number of challenges in ice modeling. Due to the remote and harsh Arctic environment, these difficulties include sparseness of in situ data. Furthermore, there is a limited amount of remotely sensed data. Of all of the unknowns, one that is particularly challenging is morphology of the underside of the icepack which actually is in contact with the ocean. This cannot be determined remotely with current technology.

B. UNDER ICE ROUGHNESS FEATURES AND DEFINITIONS

Pressure ridges are formed in the Arctic Ocean when two ice floes are forced together by wind or current. During the collision, areas of thin ice between the floes are crushed and sometimes even the edges of the floes themselves fracture. This material accumulates and piles up so as to form a ridge visible from above the ice. An approximate mirror image (but much larger in size) also forms as an inverted ridge protruding downwards into the ocean away from the underside of the ice floe. This submerged feature is referred to as an ice keel. It has been estimated that pressure ridges and their associated ice keels account for approximately half of the ice volume in the Arctic Basin (Davis and Wadhams, 1995).

C. SIGNIFICANCE

Ridging events influence the magnitude and direction of ice motion. Pressure ridges cause an increase in the aerodynamic drag at the air-ice interface and their associated keels cause an increase in hydrodynamic drag at the ice-water interface. If an ice keel is deep enough it can generate internal waves at the pycnocline, exerting much higher drag forces. This can lead to the phenomenon referred to by Ekman as “dead water” (Wadhams, 2002). This occurs in highly stratified areas where much of the energy used by a ship for propulsion is lost due to the formation of internal waves as the keel plows through the pycnocline. This loss of momentum to internal wave generation complicates modeling of the total air-ice-ocean momentum budget, especially when the size and frequency of the keels is unknown.

It is also important to note the flow effects induced by ice keels. The ratio of a keel depth to the depth of the oceanic boundary layer is very large and can even exceed one, as was the case at the Applied Physics Laboratory Ice Station (APLIS)-2007. This makes a field of large ice keels analogous to a large mountain range in the atmospheric boundary layer. Keels can cause flow acceleration, blocking and stagnation along with turbulent fluxes of heat, salt, and momentum. Simulations indicate that the turbulent wakes generated as ice keels are pushed through the water can extend several hundred meters downstream. Large Eddy Simulation modeling has shown that a 10m deep keel can cause a five-fold increase in heat flux (Skillingstad et al, 2003).

There are engineering applications which need to account for ridging. Ice ridges are the deciding factor in determining strength requirements for Arctic offshore platforms and icebreaker hull design. The depth of ice keels and their potential to scour the bottom in shallow water determines the depth of pipeline burial (Wadhams, 2002).

There are significant naval applications as well. Safety of submarine navigation in the shallow waters of the Arctic shelf and ability of a submarine to surface through the ice are affected by ice keels. Possibly even more important are the acoustic effects attributed to ice keels. Due to its density structure, the Arctic Ocean is characterized as an upward refracting acoustic environment (Fig. 1). Acoustic energy gets turned towards

the ice where it hits and is scattered as a function of the ice bottom roughness (Fig. 2). An even more extreme case is where an ice keel is deep enough to cause blocking of the acoustic path (Bourke and McLaren, 1992). The acoustic shadows cast by an extremely deep keel make it possible for a submarine to hide in its lee, shielding it from active sonar. Also of significance to submarine operations is the ambient noise of the ice pack itself. High levels of ambient noise are associated with ice floe collisions, especially at the ice edge (Wadhams, 2002). This phenomenon could greatly complicate passive sonar detection.

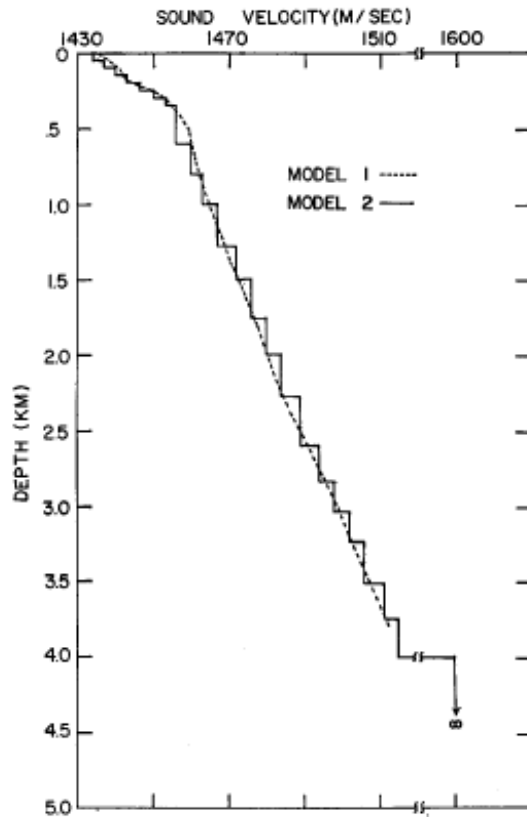


Figure 1. Simplified Arctic sound speed profiles. Model 1 is based on a sequence of plane parallel layers each with a constant gradient whereas Model 2 is based on a series of flat layers of constant velocity and density (Kutschale, 1969).

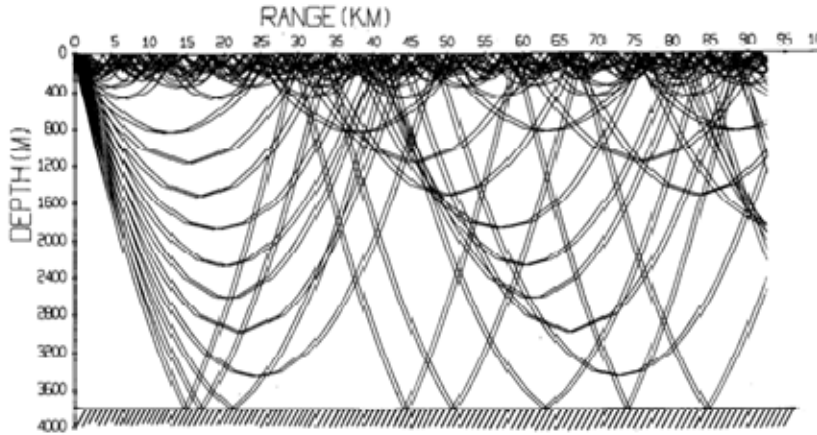


Figure 2. Acoustic ray paths for a source at 100m depth using Model 1 from Fig. 1 (Kutschale, 1969).

The effects of ridging may extend to mechanisms important to climate change. The more ridged the ice is, the greater the volume of fresh water that can cross flux gates such as Fram Strait. Ridging also increases the melting rate of ice, by increasing the surface area of the ice in contact with the warmer ocean underneath. If an ice keel is deep enough, it can cause deeper (warmer) water to be dragged up behind it and subsequent turbulent mixing will bring this warm water into contact with the underside of the ice, further melting the ice from below. Observational data support the assertion that ridged ice melts faster than undeformed ice (Davis and Wadhams, 1995).

D. STUDY OBJECTIVES

The purpose of this study was to produce a two-dimensional (2D) spectral representation of ridge properties and roughness of the underside of Arctic sea ice which would allow determination of anisotropy. The spectral approach makes it possible to determine preferred direction, wavelength, and magnitude of the roughness. If the roughness is isotropic, coupled air-ice-ocean models can reliably use a single coefficient for roughness, regardless of the direction of the wind-forced ice motion. However, if the roughness is anisotropic, directionally variable, direction-dependent coefficients may be necessary to accurately simulate ocean-ice exchange rates. This study combines moored upward looking sonar (ULS) derived ice draft data with motion determined from drifting buoys to sparsely sample and develop 2D spectra of under-ice roughness topography.

THIS PAGE INTENTIONALLY LEFT BLANK

II. DATA SELECTION

A. ICE DRAFT DETERMINATION

Significant efforts have been made to infer under-ice topography from airborne laser techniques. There have been simultaneous submarine upward looking sonar and LIDAR equipped aircraft transits that attempted to establish relationships between the two surfaces. While there was some success, the amount of snow cover is variable and difficult to determine, thus contaminating the freeboard to draft ratio for the ice alone (Wadhams, 2002). A typical ratio used as a “rule of thumb” for ice keel draft to ridge height is 3.2:1. Recently, measurements of a ridge at APLIS 2007 did not follow the relationship. A hole was melted through the ice near an ice ridge to deploy instruments. The ice was approximately 13.5m thick, which suggests that the hole went through the ice keel itself. The associated pressure ridge had a maximum surveyed height of 2.88m above sea level, implying that an its underlying keel would be on the order of 9.2m depth (Fig. 3). Even if the tip of the keel had been offset from the ridge through some sort of shearing or rafting event, it still would not closely follow the ratio. Furthermore, any mirror image of ridge and keel geometry would to some extent be distorted for multiyear ice, which has undergone annual cycles of melting and freezing cycles, along with mechanical stress and strain events and their subsequent deformation. This observation shows significant differences between ice keel and surface ridge structure.

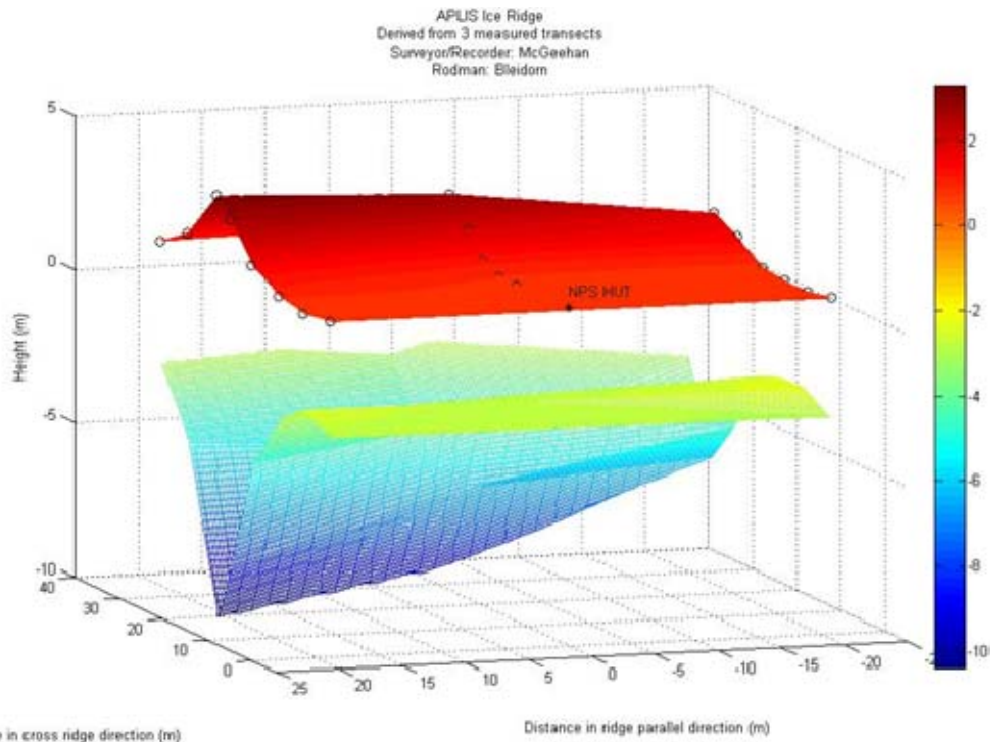


Figure 3. Surveyed ice ridge from APLIS 2007 and an extrapolated ice keel using the standard ratio for ice keel draft to ridge height of 3.2:1.

There are two common methods of obtaining reliable ice draft distribution data, both of which use ULS. One method is to mount an ULS on a submarine which then operates under the ice, recording ice draft as it goes. The second method is to mount the ULS to a bottom mooring which extends to within about 50m of the surface and record the ice draft which comes into its field of view. There are strengths and weaknesses in both methods.

1. Submarine Data

The strength of submarine data is that it can give a near-instantaneous snapshot of a broad area because the submarine can move quickly in relation to the speed of ice motion. During submarine missions, ULS data storage and power requirements are not major concerns.

However, submarine data have a number of limitations. Data can be contaminated by vessel depth or speed variations. Submarine cruises are spatially and temporally sparse. The areas surveyed are rarely if ever repeated. Furthermore, except for the SCICEX missions, collecting environmental data is not the submarine's primary mission and therefore quality may suffer somewhat.

Submarine ULS data are rarely released publicly due to security issues concerning sovereignty of territorial waters. Submarine datasets were rarely released to the public before Al Gore, then Vice President, petitioned to declassify data in an area which has become known as the "Gore Box" (National Science Foundation, 1998). This release area has since been expanded by the Chief of Naval Operations beyond the original "Gore Box" (Fig. 4) (National Snow and Ice Data Center, 2006).

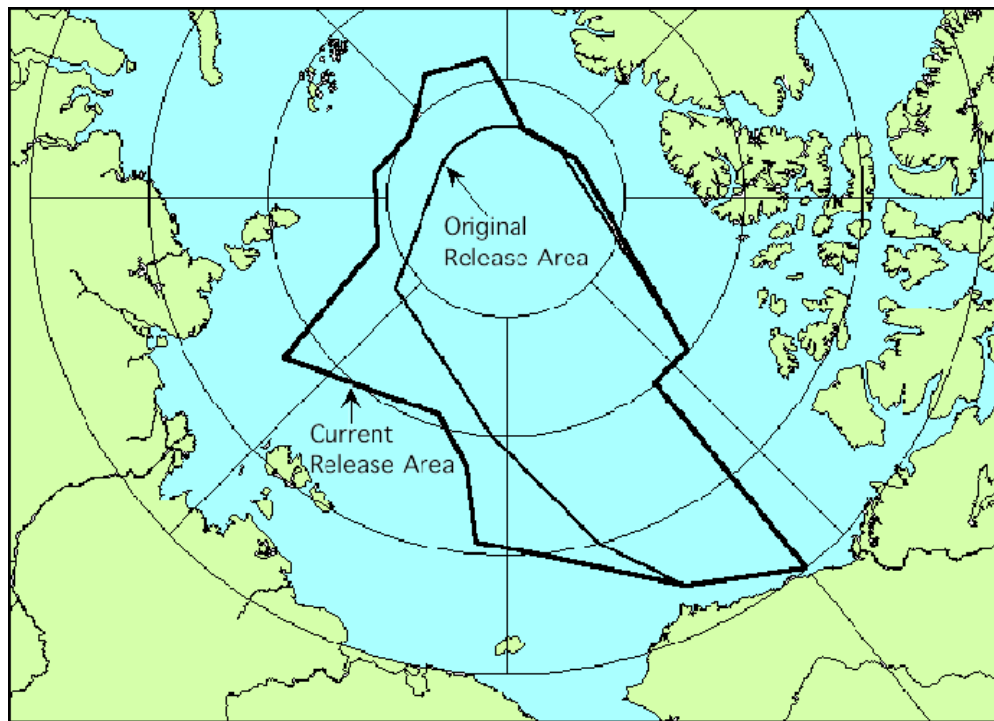


Figure 4. Original "Gore Box" and current release data for some submarine collected upward looking sonar ice draft data (National Snow and Ice Data Center, 2006).

There are additional safety issues to consider. It is dangerous for a submarine to be in shallow water under the ice with little room to maneuver. For example, USS

SARGO (SSN 583) damaged her sail in a collision with an ice keel in the shallow and confined waters of the Bering Strait during the winter of 1960 (Fig. 5) (Nicholson, 2008).



Figure 5. Crewmembers inspect sail damage on USS SARGO (SSN-583) after colliding with an ice keel in the Bering Sea in February 1960 (Nicholson, 2008).

2. Mooring Data

Mooring mounted ULS allows for the collection of a long term record of sea ice draft. The locations are usually re-occupied so multiple years of data can be collected in this manner. It is cheaper and safer to deploy a mooring than to operate a nuclear submarine. Moorings can be located in the very shallow waters of the continental shelf where submarines cannot operate. Finally, these types of datasets are not classified.

Moored ULS has weaknesses too. Temporal coverage is good but spatial coverage is limited to a single point for each mooring. The unit must be completely self-contained and rugged enough to survive the harsh conditions, placing restrictions on memory capacity and power requirements. Another weakness is that the data cannot be examined during the period of collection. The failure of a unit will not be apparent until recovery, which is typically a year after deployment.

After comparing the available submarine-mounted and moored ULS data sets, it was decided to use the moored ULS data because the observations were recent, year-round, and available for a number of different locations. These attributes make seasonal, annual, and regional comparisons of under-ice roughness possible. Specifically, the data used in this project were from the Woods Hole Oceanographic Institute's Beaufort Gyre Exploration Project (BGEP) (Proshutinsky, 2008).

B. CONVERTING TO A SPATIAL SERIES OF ICE DRAFT

The BGEP moored ULS provide time series of ice draft, $z(t)$. However, determination of isotropy requires a 2D spatial determination of ice draft, $z(x,y)$. To convert from one to the other, the time series is multiplied by the sampling rate and advection speed of the ice. Therefore, the motion of the ice needed to be determined.

C. ICE MOTION DETERMINATION

Ice motion can be derived from a variety of methods. These include Eulerian measurements with an acoustic Doppler current profiler (ADCP) pointed upwards from a fixed location, Lagrangian motion determined from drifting buoys, and satellite remote sensing products.

Ideally, there would be an ADCP collocated with every ULS to give high resolution local ice motion. Unfortunately, this type of data is not always available. For this project, ice motion was determined from the position fixes of buoys coordinated by the International Arctic Buoy Program (IABP) (Rigor, 2002). This buoy-derived motion was preferred over a number of satellite products such as those derived from AVHRR, scatterometry, and other merged datasets because of its higher temporal and spatial resolution (Fowler, 2003). Most satellite products give averaged 12 or 24 hour motion fields. However, in order to measure 2D under ice roughness, the motion vectors had to be available with a temporal resolution on the order of one hour so that the frequently dominant ice motion at these latitudes, inertial oscillations, could be resolved. This high resolution data could only be obtained from the IABP buoys.

THIS PAGE INTENTIONALLY LEFT BLANK

III. DATA PROCESSING

A. ICE DRAFT DATA PROCESSING

As part of BGEP, three ULS units were mounted on fixed moorings (referred to as ‘A’, ‘B’, and ‘C’) under the ice of the Beaufort Gyre (Fig. 6).

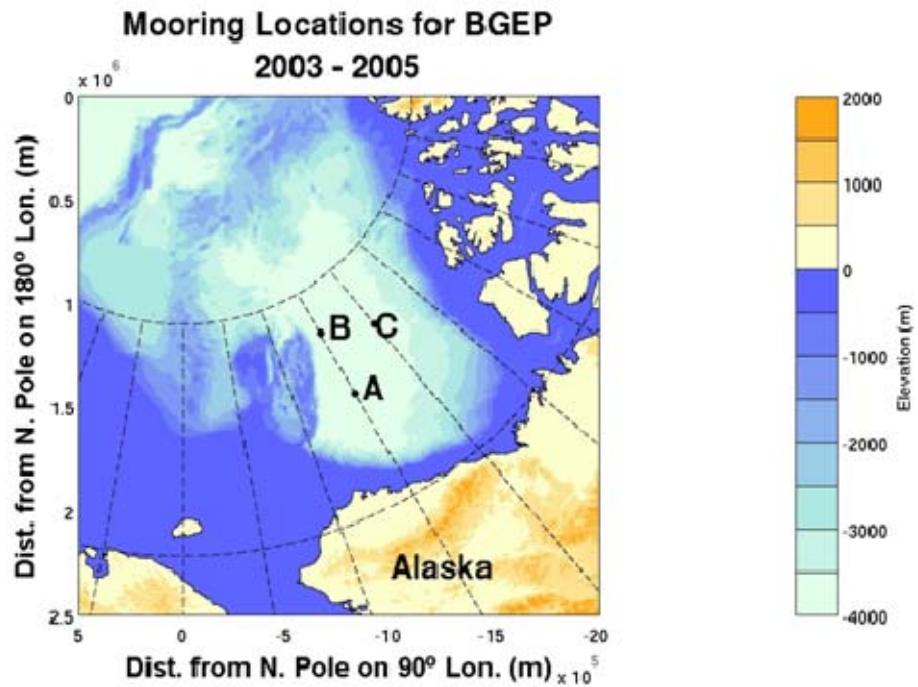


Figure 6. BGEP Mooring Locations.

The moorings were anchored in water over 3500 m deep, with the uppermost instrument on the mooring being the ULS, which was located approximately 50m below the ice bottom (Fig. 7). The ULS instruments used were ASL Environmental Sciences model IPS-4, which operated at a frequency of 420 kHz with a beamwidth of 1.8 degrees, yielding a footprint on the underside of the ice of about 2m. Range between the ULS and

the ice bottom was sampled at 2 seconds. Total hydrostatic pressure and water temperature were sampled every 40 seconds (Krishfield and Proshutinsky, 2006).

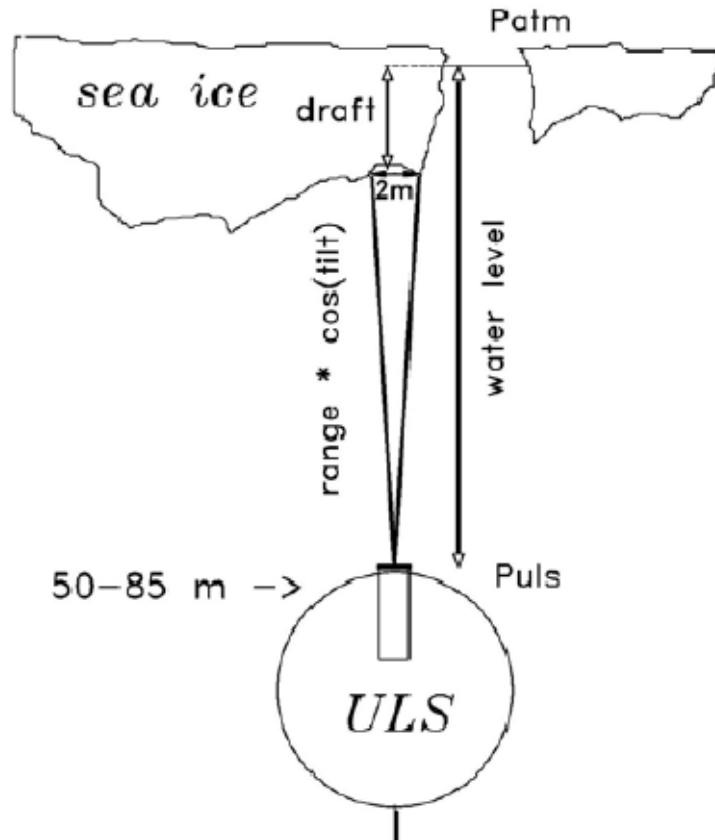


Figure 7. Schematic of ULS mooring (Krishfield and Proshutinsky, 2006).

In general, ULS data require significant processing and despiking before they are usable. For this project in particular, ice draft was calculated by correcting the measured range for tilt and sound speed variations and then correcting the total hydrostatic pressure measured at the transducer for variations in atmospheric pressure and changes in seawater density. Sound speed and density are only determined from CTD casts at the beginning and end of the deployment. During this deployment, it was impractical to have a CTD continuously profiling so other methods are required. Temperature measured at the ULS can locally correct sound speed and density, while corrections can also be determined by using the range observations during periods of open water (where $draft=0$). However, this method has limitations because it is often difficult to distinguish frazil and thin ice from open water. Since in situ observations of atmospheric pressure are very sparse in

the polar regions, they were obtained from NCEP sea level pressure reanalysis data. After all corrections have been made, draft calculations have an error of $\pm 5-10$ cm. (Krishfield and Proshutinsky, 2006).

A large source of error in all ULS observations is the finite beam width of the transducer. Although it is assumed that the draft value assigned to a particular location on the ice is along the transducer's axis, this is not always the case. On sloping features, the first return of the sonar pulse may be due to an off axis feature which is shallower. This will cause the apparent draft at a point to be greater (Fig. 8). The net effect is to overestimate ice draft and to broaden the apparent width of features (Melling et al, 1995). The only way to mitigate this effect is to use an ULS with as narrow a beam width as possible. The IPS-4 transducer has a beamwidth of 1.8 degrees which is narrow in comparison to sonars used to generate previous datasets, which used beamwidths on the order of 14 degrees (Wadhams, 1978).

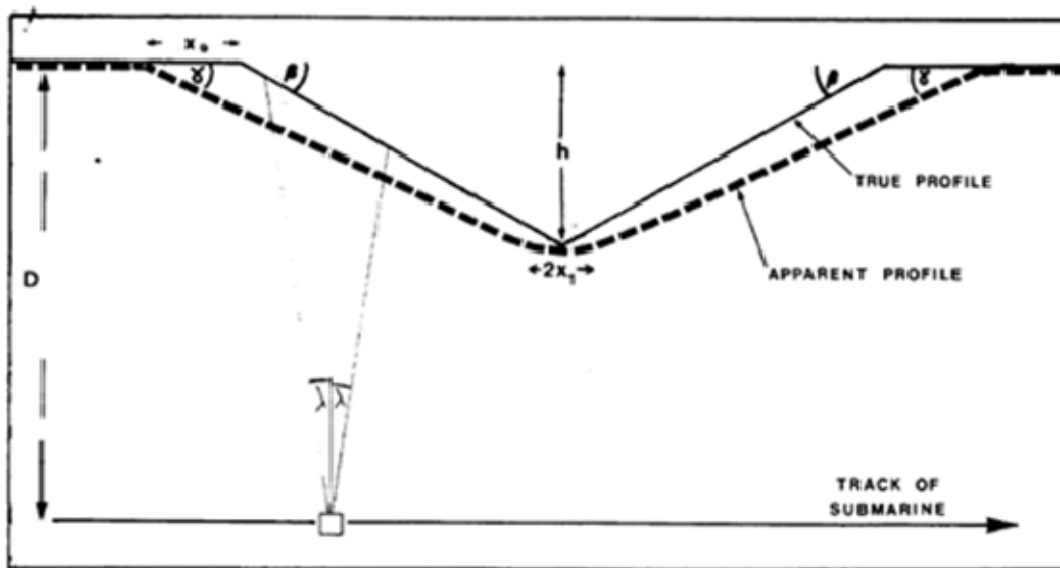


Figure 8. Effect of echosounder beam width on apparent keel profile. Note that the apparent width and average draft increase (Wadhams, 1978).

Other sources of error are due to phenomena occurring in leads. Waves can give an apparent draft if sampling occurs while its trough is over the ULS. Likewise, the crest of a wave can give a solution with a negative draft, which would physically mean the

sonar was looking out of the water. Another effect is from wave breaking, which can inject clouds of bubbles into the water. These in turn may appear as legitimate ice drafts in the sonar record (WCRP, 2004).

Another major complication in interpreting ULS observations is the effect of pressure ridge orientation relative to the direction of sampling. If a keel is sampled perpendicular to its axis of lineation, there is no problem. However, if the keel is sampled at some other angle, the effect is that the keel appears to be broadened and the spacing between features of similar alignment is lengthened as well (Fig. 9 and 10). The wavelength will always appear lengthened; it cannot appear shortened. This leads to a “reddening” of the spectra whereby actual wavenumbers are shifted to lower wavenumbers. The most extreme case occurs when sampling along the axis of a keel, where the wavelength or spacing between keels becomes infinite and wave number goes to zero.

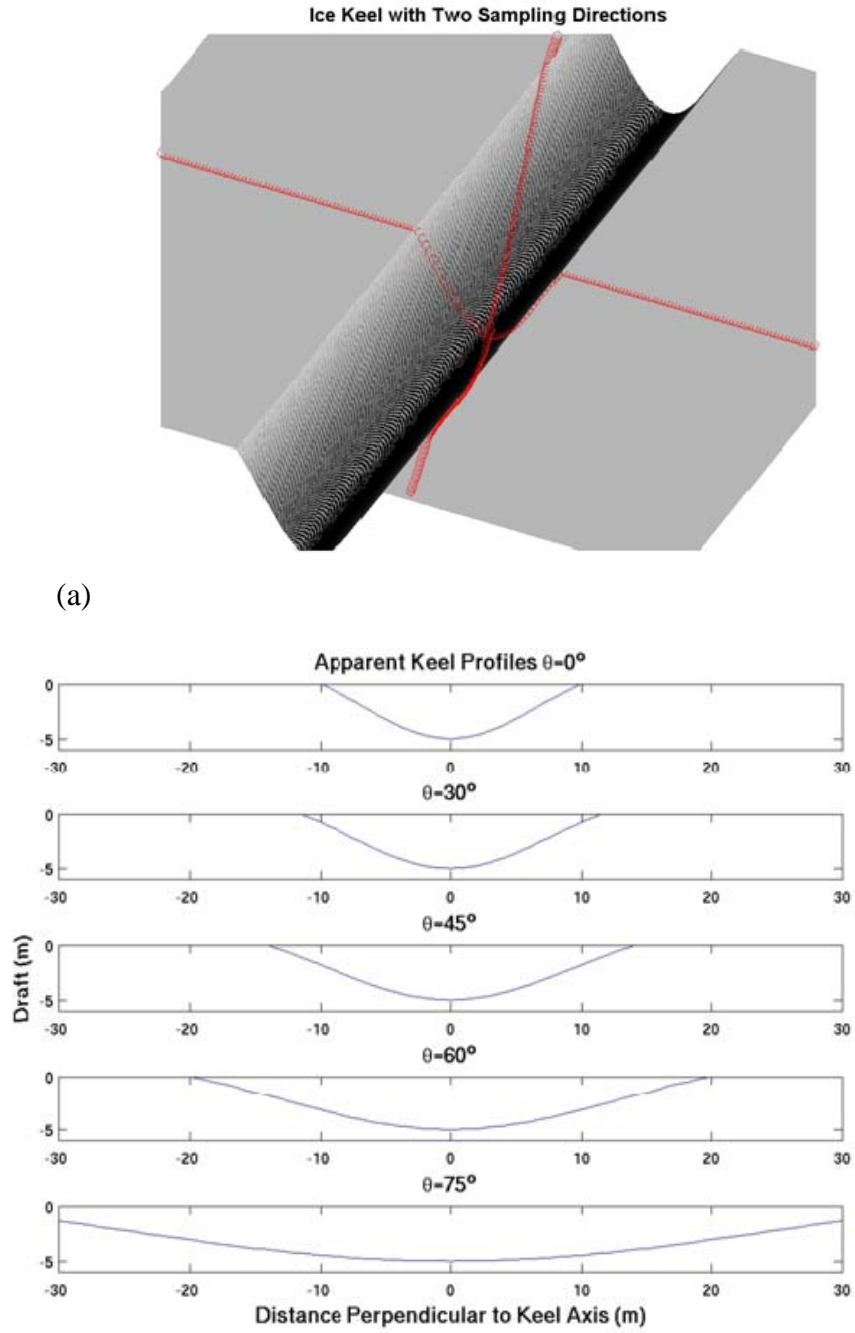
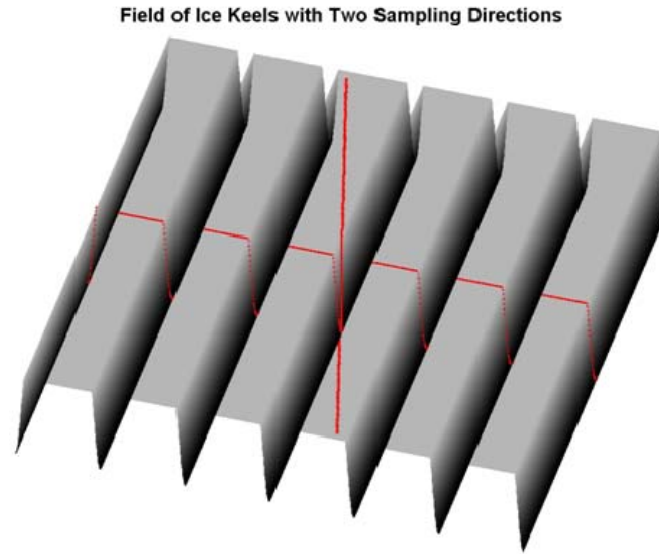
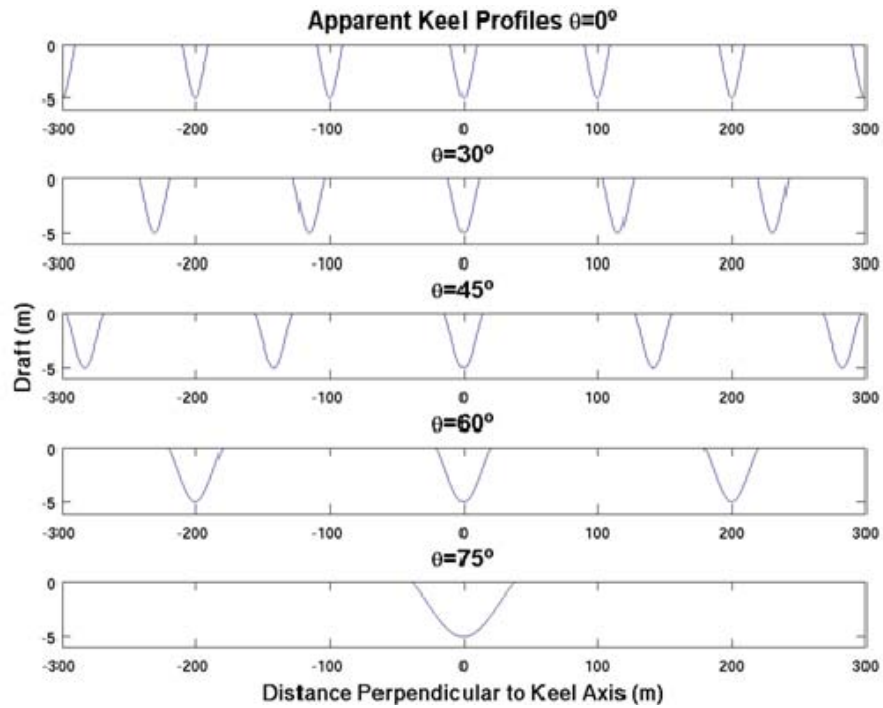


Figure 9. (a) View from below ice keel showing sampling directions perpendicular to the keel and cutting across it at 75° . (b) Apparent keel profiles as a function of sampling angle. $\theta = 0^\circ$ and $\theta = 90^\circ$ correspond to sampling directions perpendicular and parallel to the keel axis, respectively. Note that the apparent width and average draft increase as the angle becomes greater.



(a)



(b)

Figure 10. (a) View from below field of keels with sampling directions 0 and 75° . (b) Apparent draft profiles from field of regularly spaced keels as a function of sampling angle. Note the increase in apparent spacing of the ice keels as the angle increases.

This problem, sometimes referred to as spatial aliasing, needs to be resolved in order to generate a meaningful 2D spectrum of under-ice roughness. As the examples (Fig. 9 and 10) above have illustrated, a 1D slice through a 2D field is reddened (except for the one case where the slice happens to be exactly perpendicular to the orientation of the field of features). This reddening occurs because the 2D wavenumber information is lost. If the whole 2D spatial field were available, obtaining a correct 2D spectrum would be easy with a 2D FFT. This project used a processing routine for sparse data in which directional information was retained in the autocorrelation function, which preserved the 2D wavenumber in the spectrum.

B. ICE MOTION DATA PROCESSING

Numerous IABP buoys passed through the area of the BGEP moorings from 2003-2005 (Fig. 11). The associated raw buoy position data were obtained from the IABP office. Each file represented one buoy and covered a period of about 1 year. The following processing routine was applied to each data file using an algorithm written in MATLAB.

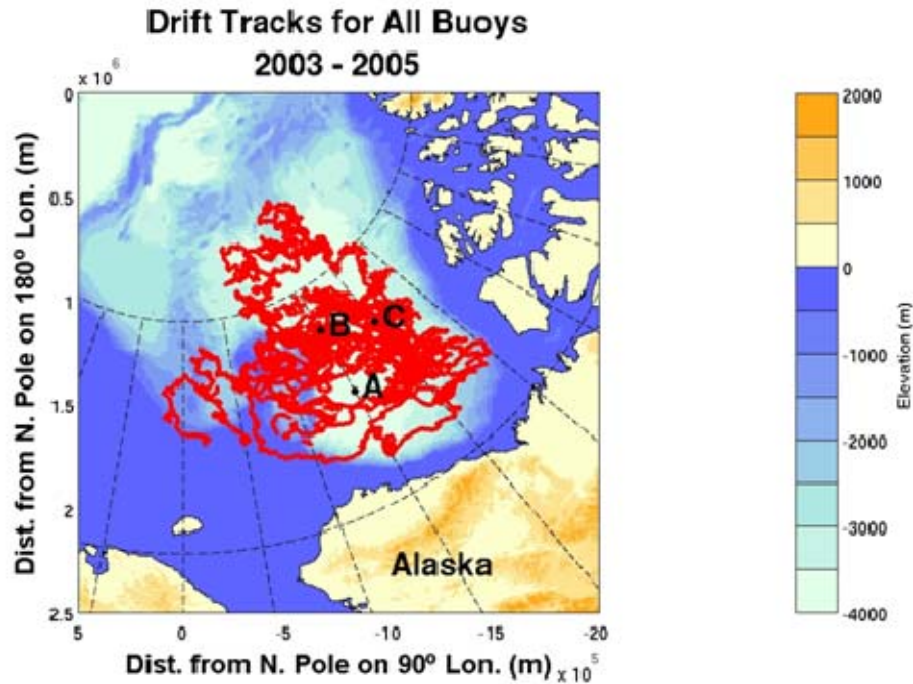


Figure 11. Drift tracks of all buoys in mooring area from 2003-2005.

First, the IABP buoy data file was loaded and all times were converted to year day referenced to 01 January 2003 as the start point. Next, redundant records were removed. The record was then scanned to find times when neither the latitude nor longitude changed for successive times. These records were removed as well. Position data were then converted from geographic coordinates of latitude and longitude to a polar stereographic grid compatible with the International Bathymetric Chart of the Arctic Ocean (IBCAO). This coordinate system is centered with the origin at the geographic North Pole. The x-axis measures distance in meters from the North Pole along the line of 90 degrees East longitude and the y-axis measures distance in meters from the North Pole along the line of 180 degrees longitude. The buoys did not report position data on a standard time schedule. Therefore, the data were interpolated onto a common hourly time vector from the start of 2003 to the end of 2005. This allowed buoy positions to be available for every hour (on the hour). The polar stereographic buoy positions were

despiked to remove anomalous position data. A remaining problem was occasional, long temporal gaps. Interpolating across these would have introduced erroneous velocity estimates. These gaps in the position time series could be due to rime building up on a buoy's GPS or broadcast antenna at some point and then getting washed off later. Significant data gaps were identified by finding position fixes that occurred more than 6 hours apart. Interpolated data between these fixes were discarded. Velocity components (u,v) were then calculated as a finite difference using $u = \frac{\Delta x}{\Delta t} = \frac{x_2 - x_1}{t_2 - t_1}$. The speed (magnitude of the overall velocity) was determined via the Pythagorean theorem.

The next task was to use the processed buoy data to generate a time series of u (east-west velocities) and v (north-south velocities) at each mooring. The following process was carried out for each mooring location.

First, the mooring's geographic coordinates of latitude and longitude were converted to the polar stereographic grid previously described. For each time step (every hour), the distance between all contemporaneous buoy positions and the mooring were calculated. All buoys within 250km of the mooring (Fig. 12) at that time were flagged and the mean of their velocity components (u,v) was then recorded as a value representative for that mooring. A time series was created at each mooring by repeating the process: advancing one time step at a time, determining the buoys within 250km, and recording the mean of their motion data.

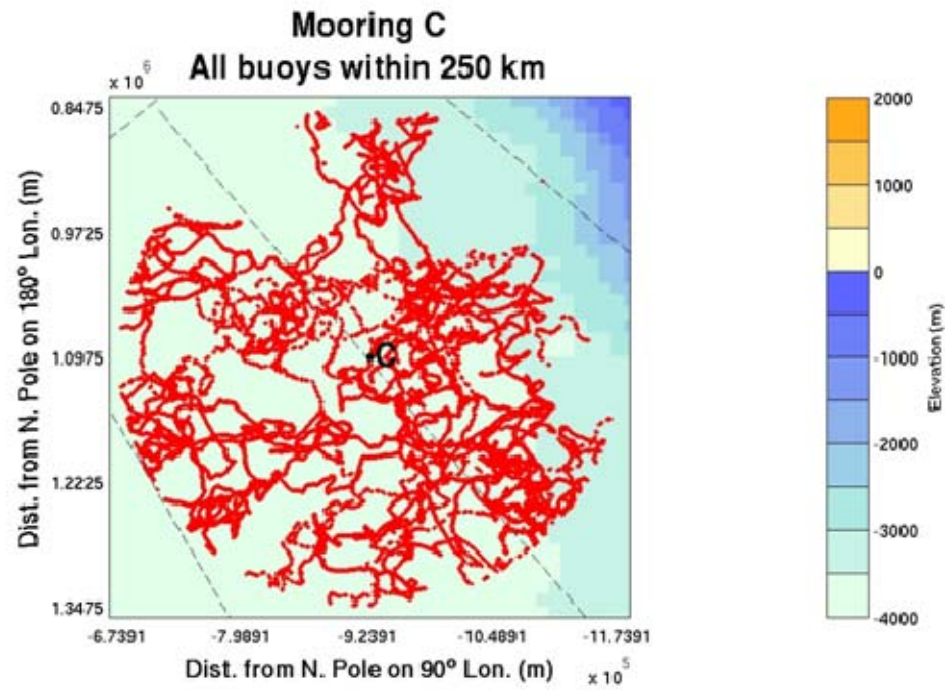


Figure 12. Tracks of all IABP buoys passing within 250km of mooring C from 2003-2005.

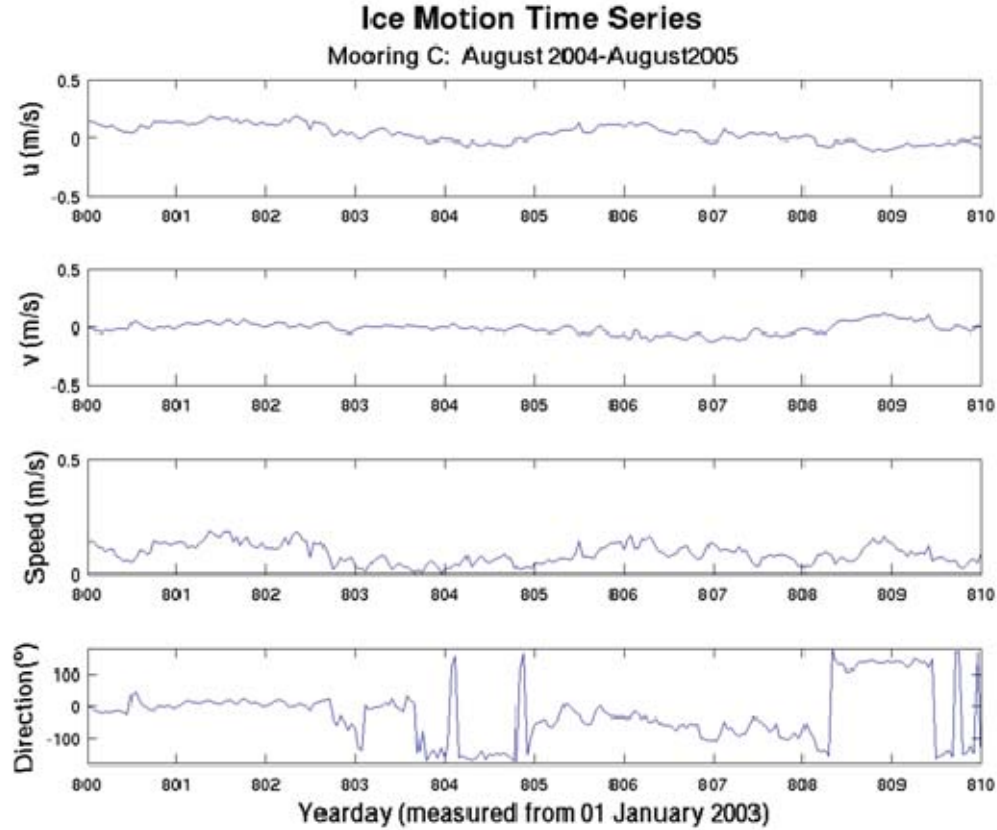


Figure 13. Example time series of motion compiled at Mooring C: August 2004-August 2005.need to correct

Note that the actual direction of ice motion for mooring C was constantly changing because of the inertial oscillations (Fig. 13). Therefore, the motion data needed to be segmented into a number of segments so that each piece was approximately unidirectional. For the entire time series of motion (at each mooring), the direction was calculated from u and v using a four quadrant arctangent function $\theta = \tan^{-1}\left(\frac{v}{u}\right)$. Hourly change in direction as well as cumulative change in direction were derived. Also, the hourly distance travelled and the cumulative distance travelled were calculated. If the cumulative change in direction or the cumulative distance travelled exceeded a threshold (defined here as 45 degrees for direction and 2,000m for distance), the segment would end with the point previous in time, so as not to exceed the threshold. The cumulative counters were reset to zero and the process was repeated. Segment start and stop times, and average speed and direction were recorded.

A limitation of this approach is that it assumes that the ice motion is continuous in space between the buoys and moorings, ignoring spatial gradients of velocity. For combining mooring and motion data, Melling et al (1995) cautioned against using Lagrangian methods such as radio beacons or GPS receivers in buoys mounted in the ice because they quickly leave the moorings behind and do not give true motion at the mooring. The error is particularly large near coastal boundaries and during the ice melt period. In this case, well away from land boundaries, it is assumed that the primary motion is due to inertial oscillations resulting from synoptic scale meteorological events of 1,000-2,500 km. With forcing of this scale, it is assumed that ice motion is continuous for a distance of 250 km.

C. COMBINING THE ICE DRAFT AND MOTION DATA

Without motion data, all that is recorded at the ULS is a time series of ice draft. The addition of motion data helps to transform this time series into a 2D spatially referenced description of ice draft. The process used below was first outlined by Hibler (1972).

For each mooring, the ice draft information was loaded and corresponding times were converted to year days referenced to 01 January 2003 to be consistent with previous data. Using each time segment derived from the motion data, the corresponding ice draft time series had its mean removed and the autocorrelation function was calculated using

$$R_{xx}(\Delta x) = \frac{1}{N} \sum_{i=0}^{N-1} f(x_i) f(x_i + \Delta x), \text{ where } R_{xx} \text{ is the autocorrelation value (in units of } m^2 \text{),}$$

N is the total number of data points, $f(x_i)$ is the value of the draft function (in units of in units of m) evaluated at x (in units of m), and Δx is the spatial lag (in units of m) (Fig. 14).

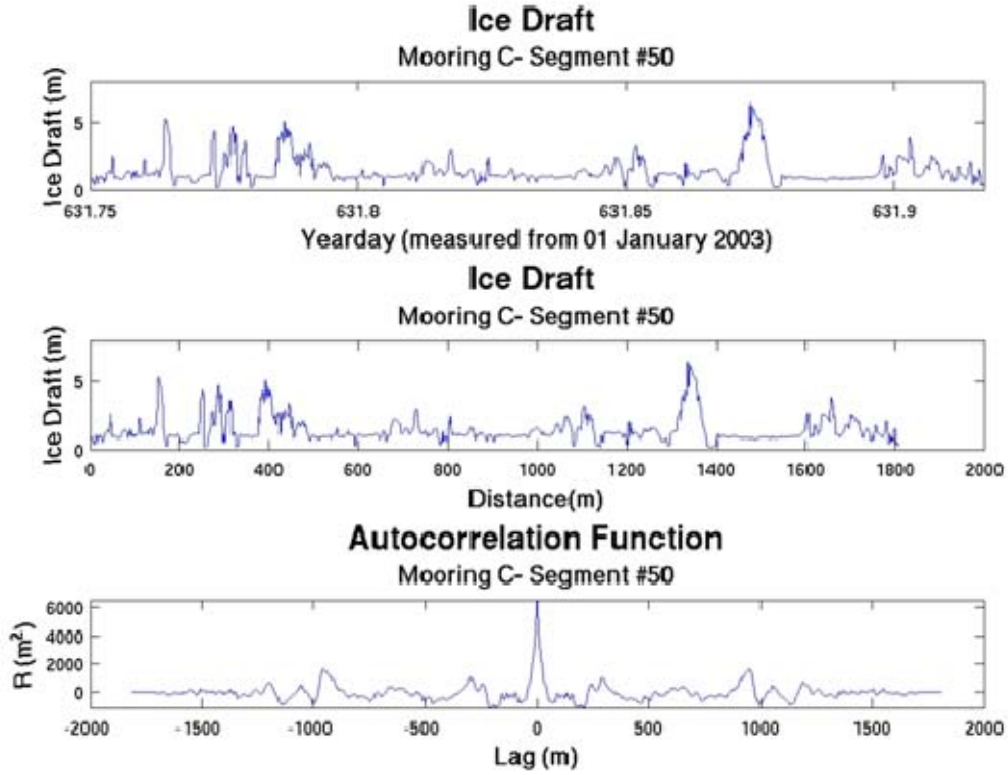


Figure 14. Ice draft time series, distance series, and autocorrelation function for Segment #50 at Mooring C.

The spatial lags Δx were a function of segment velocity. These lags were calculated using $\Delta x = \Delta t \cdot \sqrt{u^2 + v^2}$, where Δt was the sampling interval (2s), and $\sqrt{u^2 + v^2}$ was the segment average speed (m/s).

For each mooring, all segment derived autocorrelation functions were then plotted together as functions of lag and segment direction. The result was a series of autocorrelation functions emanating radially from the mooring like spokes of a wheel (Fig. 15).

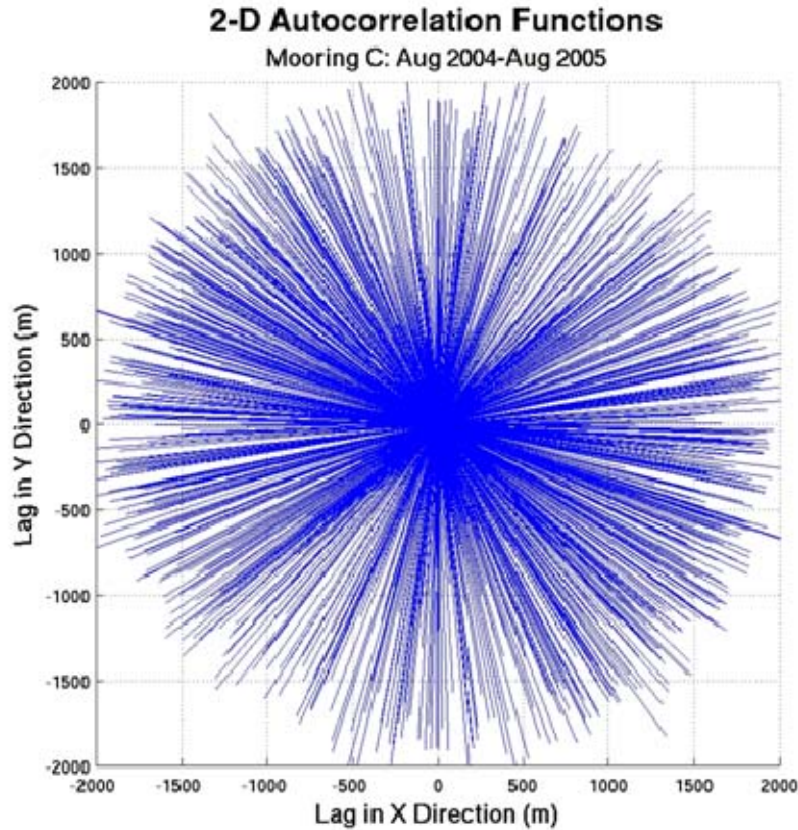


Figure 15. Combined autocorrelation spatial coverage.

It is important to note that the process used here departed from the one outlined by Hibler. Hibler recommended normalizing the autocorrelation functions. However, normalization strips away the total variance, which is critical for interpreting spectra. Normalized autocorrelation functions are unable to tell the difference between small and large roughness elements. The large elements, the ice keels, need to be distinguished. Their effects are distinct from roughness elements of a much smaller centimeter scale. A field of small roughness elements oriented in one direction could dominate a normalized 2D spectrum, even though there was a more sparse field of very large roughness elements at a different orientation which in reality dominates the physical processes. Hence, in this study, variance was conserved (i.e. the autocorrelations were not normalized) in order to make direct comparisons between different locations, times, and directions.

It is also important to note that this step of combining the autocorrelation functions is crucial because it mitigates the effects of sampling across features at an

angle. The relative change in autocorrelation functions between high and low lag numbers is determined by the direction that the linear ridge feature is crossed. By using the autocorrelation function and referencing it with its direction, the subsequent 2D spectrum does not become reddened because the 2D wavenumber is conserved. Energy peaks will occur at the correct wavenumbers even though the field is sparsely sampled. This is demonstrated with test cases in section III A.

This combined autocorrelation function is an intermediate step. The desired final product is the 2D spectrum. Since the autocorrelation function and the spectrum are a Fourier transform pair, it is straightforward to go from one to the other using the Fast Fourier Transform (FFT). However, the data needs to be on a continuous grid in order to use the FFT. The autocorrelation function had some gaps in coverage and so needed to be processed to be ready for the 2D FFT.

The next step was to combine all of the autocorrelation functions by binning them in polar coordinates. The bins chosen were 10 degrees wide and 5m long to achieve satisfactory point density. It became apparent that each autocorrelation function had to be interpolated onto a common vector in order to keep the spacing of the points constant when compared to the other functions. It was observed that due to the fixed sonar sampling rate of 2s, autocorrelation functions corresponding to periods of slow ice motion had their data points spaced much more closely together than did functions from periods of faster ice motion. The result was that a particular bin might have 10 points from the slower autocorrelation function and only 1 point from the faster one, even though they both crossed the bin at the same angle. The value subsequently assigned to the bin was biased in favor of the slower moving segment of data. The autocorrelation data was therefore interpolated onto vectors of common length and point spacing, specifically 2000m and 0.5m respectively. This issue of oversampling during periods of slow ice motion and undersampling during periods of fast ice motion was addressed by Melling and Riedel (1995) who showed that resampling at a constant spatial rate was more appropriate than using the time series when trying to derive independent data for statistical comparisons. The mean was taken for each bin and its value was assigned to a point at the bin's center. These binned data were then interpolated and transferred from

the polar coordinate system to a Cartesian grid measuring from -1300 to 1300 m in both x and y directions with grid points every 5m. The 2D FFT of the 2D autocorrelation function was taken to obtain a 2D spectra using

$$S(k, l) = \frac{1}{N^2} \sum_{i=0}^{N-1} \sum_{j=0}^{N-1} R(\Delta x_i, \Delta y_j) e^{-2\pi i(k_x \Delta x_i + l_y \Delta y_j)},$$

where k and l are the horizontal and vertical wavenumbers, Δx_i and Δy_j are the lags in the x and y directions, and R is the value of the binned and interpolated 2D autocorrelation function described above.

The highest resolvable wavenumber, the Nyquist wavenumber was $k_{Nyquist} = \frac{1}{2 \cdot \Delta x}$, where Δx = grid spacing (5m). This corresponded to a wavelength of 10m, which was expected to be sufficient to characterize the rapidly changing portion of the under ice environment.

Synthetic data was created from a known field in order to test all phases of the process (see section III for detailed results). The process showed itself much more sensitive to variations in angular rather than radial bin width. Decreasing angular resolution caused the spectra to get smeared out. Increasing it caused critical decreases in point density in the initial binning process due to the sparse nature of the data. Radial variations had little effect on the spectra. However, as the radial resolution increased, there was not enough point density to fill every bin. If it decreased, the ultimate resolution of features occurring with higher wave numbers was decreased and roughness on these scales cannot be determined. In the end, both angular and radial resolutions used were a compromise in the fact that they had to remain coarse enough to deal with the sparse data.

The size of the 2D autocorrelation area taken for the 2D FFT was determined by the length scale of the phenomenon occurring with the lowest wave number. This phenomenon was assumed to be distinct ice keels. Historical data shows the spacing between distinct ice keels has over a 99% probability of being less than 1000m (Fig. 16) (Wadhams and Davy, 1986). Therefore, the output from the FFT would need to be able to resolve a wave number of 0.001m^{-1} . Using $resolution = \frac{1}{N \cdot \Delta x}$, it follows that for a field

with grid spacing Δx equal to 5m, the required resolution of 0.001m^{-1} can only be achieved if the number of points N is greater than or equal to 200. This forces the size of the field to go into the 2D FFT to have a radius of at least 1000m and the field to measure at least 2000m across.

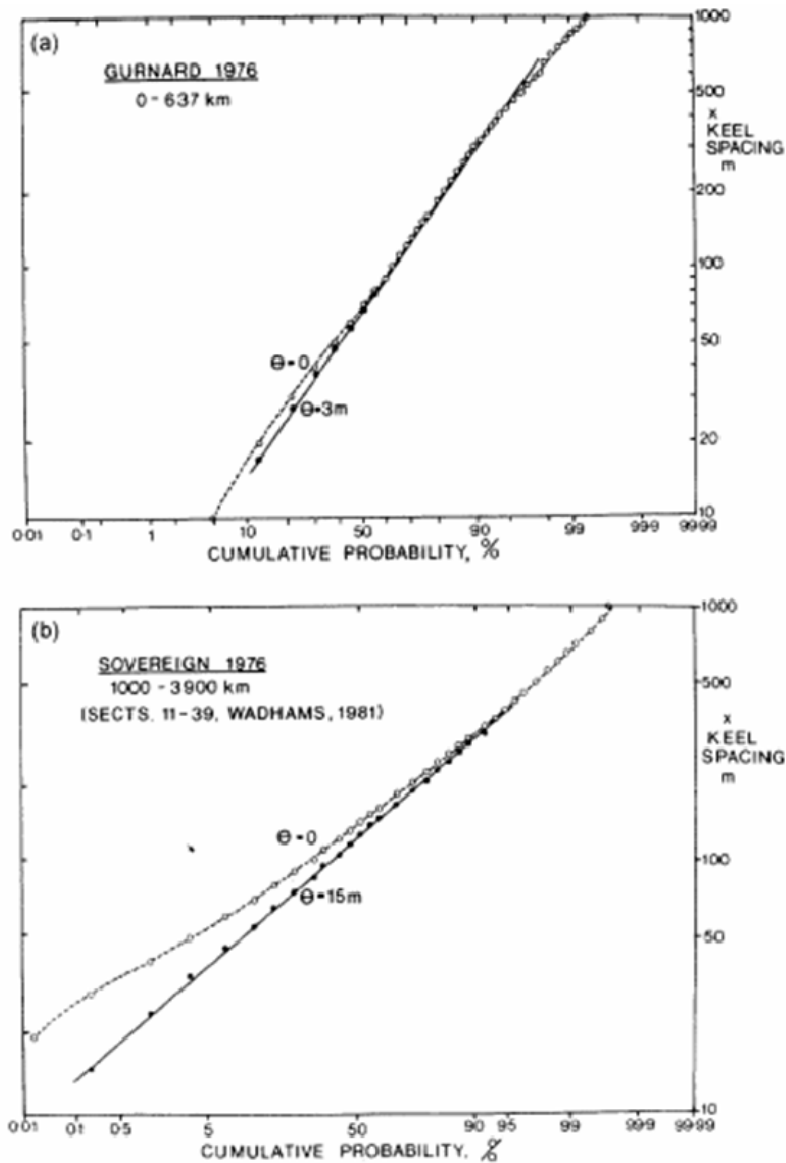


Figure 16. Cumulative distribution functions of ice keel spacing. Plot (a) is derived from narrow beam sonar in the Beaufort Sea: open circles have a threshold of 0m and closed circles have a threshold of 3m. Plot (b) is derived from wide beam sonar in the Eurasian Basin: open circles have a threshold of 0m and closed circles have a threshold of 15m (after Wadhams and Davy, 1986).

Even when using the synthetic data of idealized cases, there were artifacts in the spectra from the processing routine. To attempt to decrease these artifacts, zero mean random noise was added to the 2D autocorrelation surface before the 2D FFT converted the field into spectra. The noise level used was 1% of the standard deviation of the entire 2D autocorrelation surface. Even with this improvement, there continued to be noise at very low wave numbers corresponding to long wavelengths. 2D convolution filtering failed to make the plots easier to interpret. Much of the noise was at wave numbers below 0.001m^{-1} , which had previously been set as the maximum length scale imposed by independent keel spacing. Therefore, although it was apparent that the process could not differentiate between the processing artifacts and real data at very low wave numbers (long wavelengths), it was considered to be acceptable because energy is not expected to be there due to the physical scaling argument.

IV. ANALYSIS AND DISCUSSION

A. TEST CASES

To confirm that the technique worked as expected and to aid the interpretation of real world data, a number of test cases were conducted where a known field of under ice features was put through the processing routine. The random fields were generated and then sampled using real ice motion observations. The segments used were from Mooring C from August 2004-August 2005. For consistency, the Mooring C trajectories were used to generate ice draft data from the known fields for all of the test cases.

1. Single Sine Wave

The first test case was that of a field created from a single sine wave with amplitude 5m, wavelength 200m, and oriented so the crests form a line running vertically across the field (Fig. 17(a)). When put through the processing routine, the autocorrelation function showed the orientation correctly (Fig. 18), and the resulting spectra put the peak energy at the correct wave number and direction, $[k,l]=[\frac{1}{200},0]$ (Fig. 17(b) and (c)).

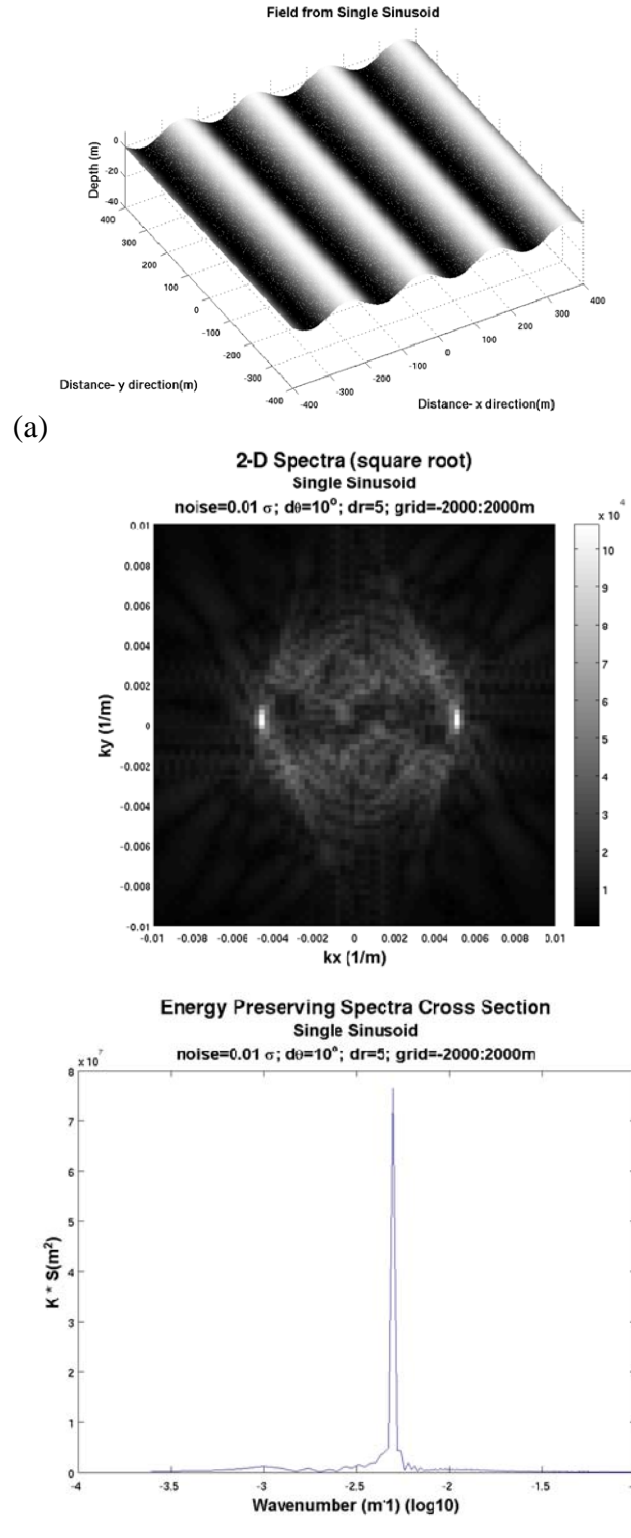


Figure 17. (a) Field generated from single sinusoid. (b) Resulting 2D spectrum with energy peaks at correct wavenumbers. (c) Spectral cross section with vertical axis scaled by wavenumber. Note peak energy at correct wave number.

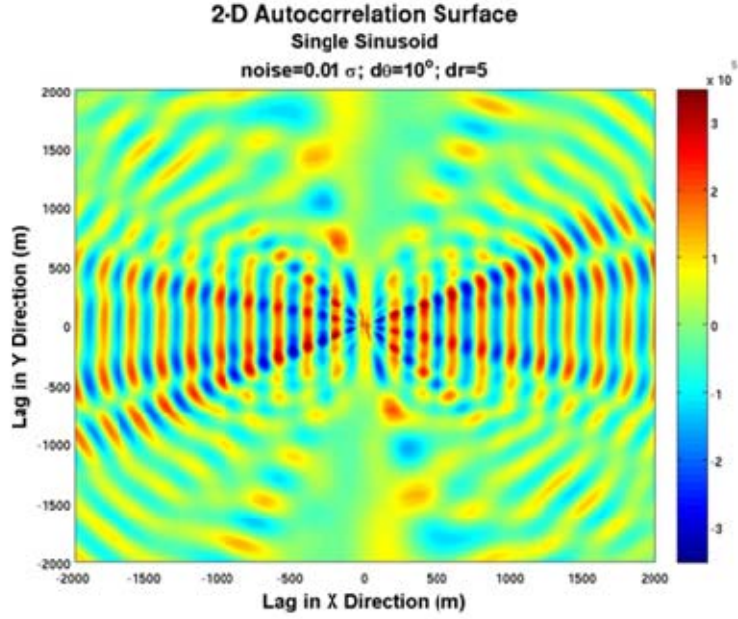


Figure 18. 2D autocorrelation plot for field created from a single sinusoid. Note the distortion caused by the angular binning process as angles come less perpendicular to the axis of the crests.

2. Single Sine Wave Derived from Different Motion Data

The second test case was another single sine wave with identical parameters as in Case 1. The object of this case was to determine if the output was independent of the velocity estimates used to translate the ULS time series into a spatial series. The identical field from Case 1 was generated but this time it was sampled by ice motion data for Mooring C from the previous year (August 2003-August 2004). Again, the spectra put the peak energy at the correct wave number, suggesting that the technique is insensitive to the details of the conversion of the time series to a spatial series with the buoy-derived velocities (Fig. 19).

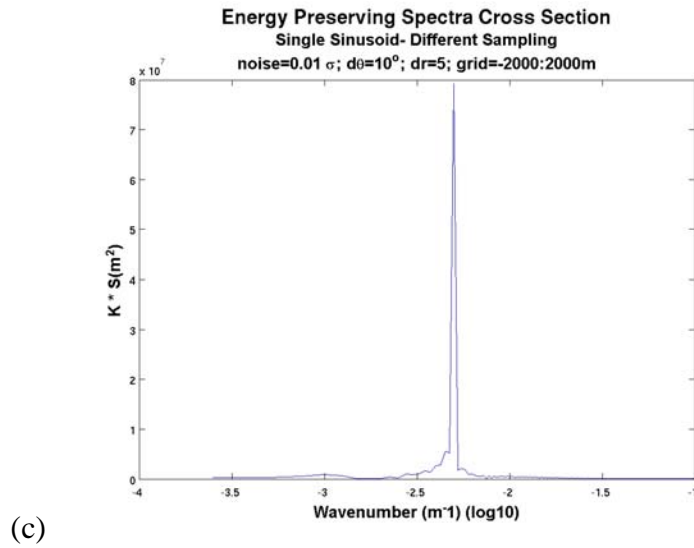
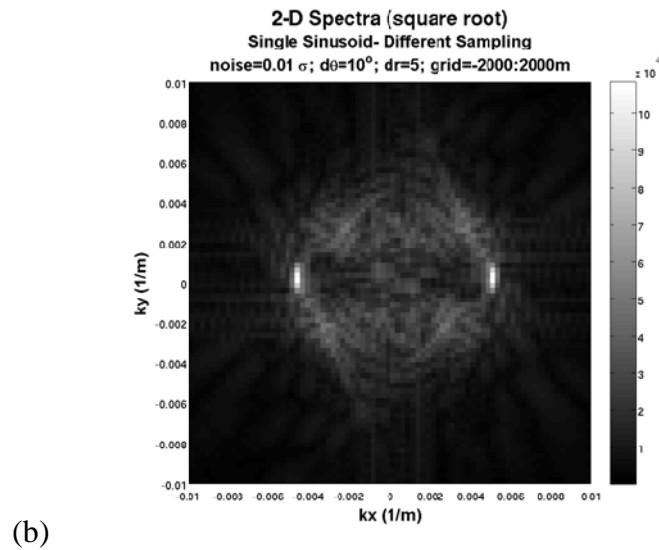
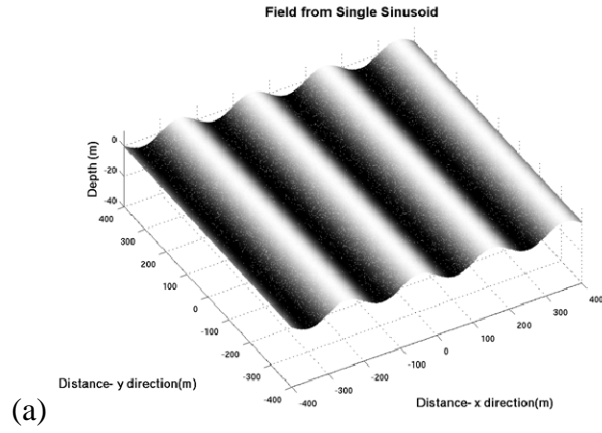


Figure 19. (a) Field generated from sinusoid. (b) 2D spectrum from field sampled with different ice motion data. (c) Spectral cross section.

3. 2 Sine Waves of Different Wavelengths but Different Amps and Different Orientation

This test case sampled a field made by combining two differing sinusoidal fields (Fig. 20). The first field had a wavelength of 200m, vertically oriented crests, and an amplitude of 5m. This corresponded to a wavenumber of $k=.005 \text{ m}^{-1}$ and $\log_{10}(k)=-2.3$. The second field had sinusoids of 500m, diagonally oriented crests, and amplitude of 20m. This corresponded to a wavenumber of $k=.002 \text{ m}^{-1}$ and $\log_{10}(k)=-2.69$.

At a glance, it may appear that only the larger amplitude wave was represented in the 2D spectrum (Fig. 21(b)). However, cross sections through the 2 directions of interest show that both sinusoids were correctly resolved (Fig. 21(c)). Not only were peaks located in the correct wave numbers, but their relative sizes were consistent with their relative amplitudes. This reflects the larger variance in larger amplitude ice keels. This was one of the most important test cases because it showed that the process is robust enough to properly display a field created from sinusoids with differing orientation, wavelength, and amplitude.

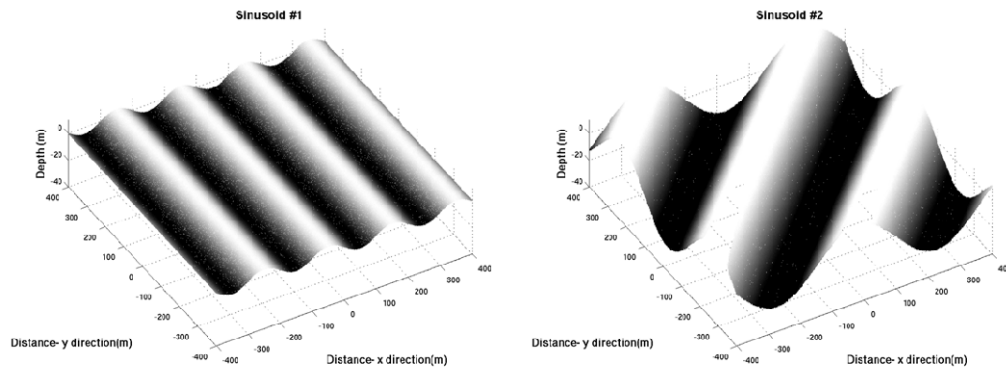


Figure 20. Sinusoids #1 and #2 which combine to make up the composite field of two sinusoids with differing amplitude, wavelength, and orientation.

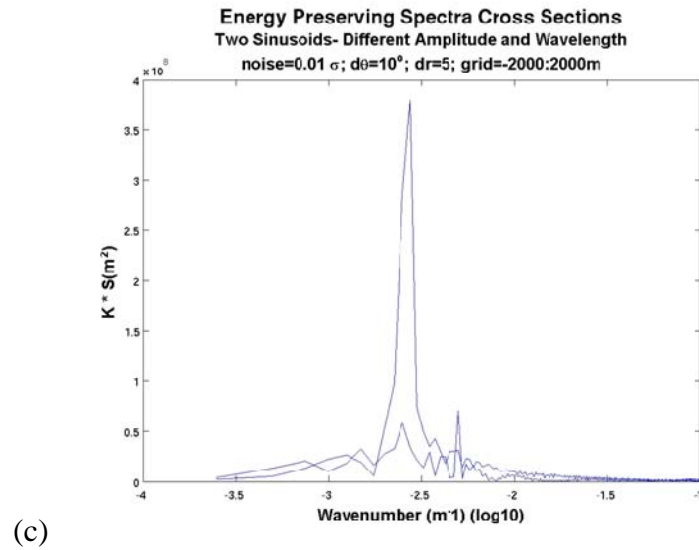
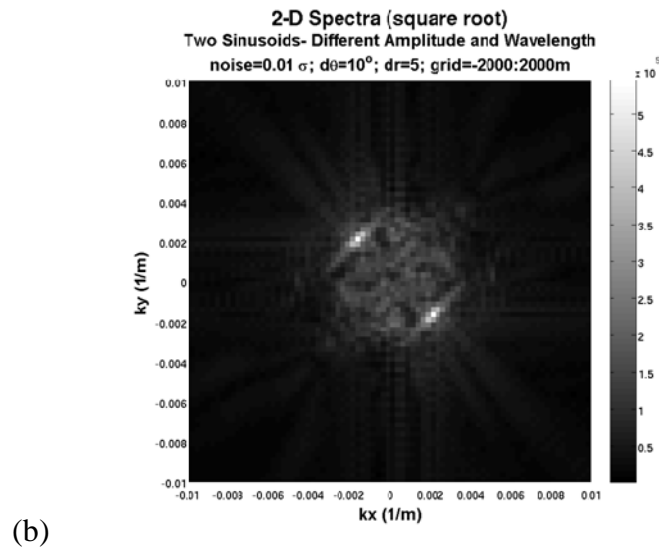
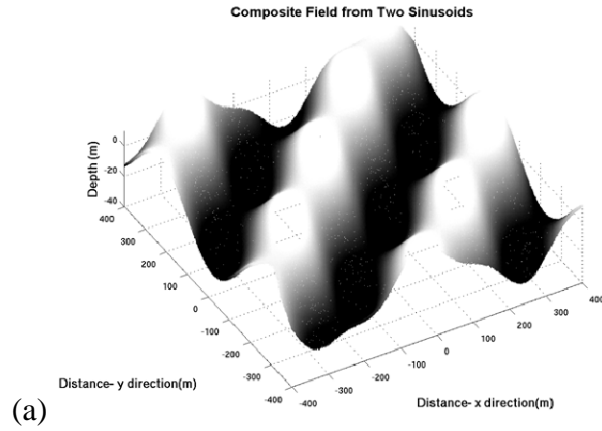


Figure 21. (a) Composite field from two sinusoids. (b) 2D spectrum of field. (c) Spectral cross sections with peak energy and relative amplitude correctly represented.

4. Single Sinc Function

This test case was to test how well the process worked on a non-sinusoidal field. A field was created with a sinc function repeating periodically with a wavelength of 100m (Fig. 22(a)). To approximate the shape of a true ice keel, the amplitude was set at 5m, it was 20m wide base. The peak amplitude of the spectra was at the correct wavenumber (Fig. 22(b)). However, harmonics were observed in the spectra (Fig. 22(c)). This is due to the nature of the 2D FFT process, which struggles to fit high wavenumber sinusoids into the observed profile. The harmonics were expected however, as the Fourier transform of the sinc function is the square wave. The implication is that the process can correctly represent non-sinusoids.

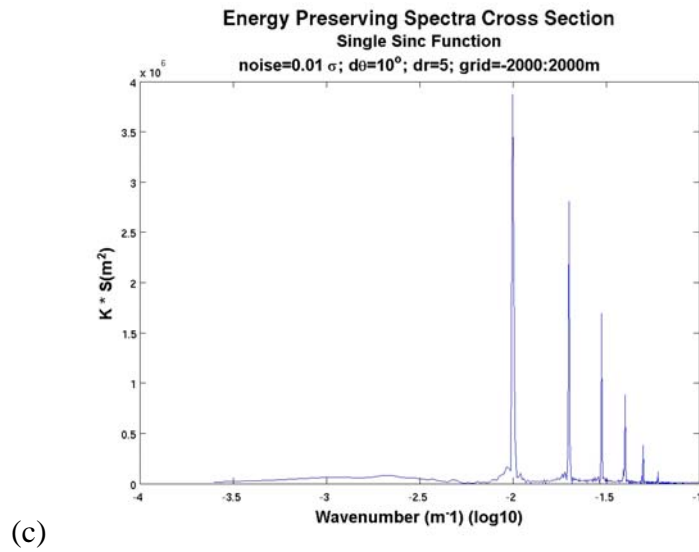
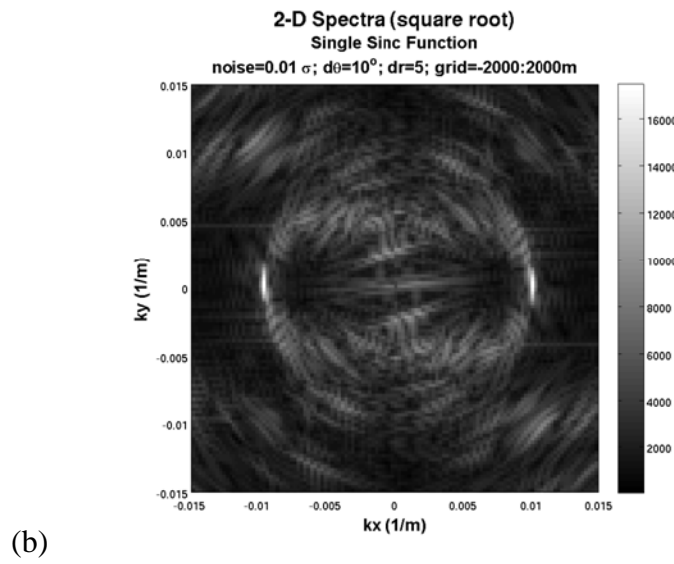
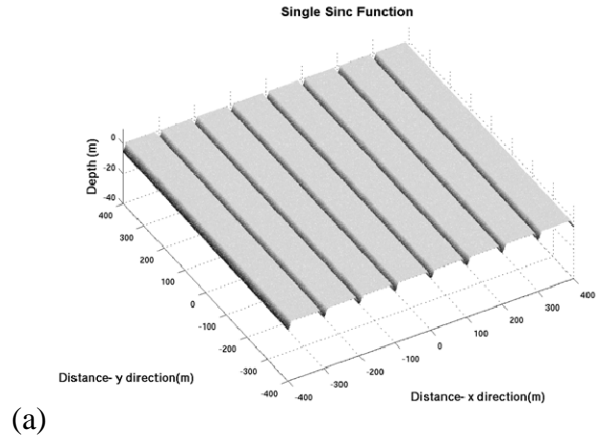


Figure 22. (a) Field from single sinc function. (b) 2D spectrum from field. (c) Spectral cross section; note the decreasing harmonics at higher wavenumbers.

B. BEAUFORT GYRE DATA

1. Mooring C: August 2004–August 2005

Mooring C had the most dense buoy coverage and is used to illustrate the Beaufort Gyre data. The case described below is from August 2004– August 2005, the second year of deployment. This dataset had the best coverage with respect to the 2D autocorrelation function and therefore is considered the most robust.

The 2D spectrum (presented as the square root of variance for display purposes) appears by eye to be directionally variable (Fig. 23a). Eight spectral cross sections taken in directions ranging from 000 to 157.5° in 22.5° intervals show that the spectra have a power law dependence on radius (Fig. 23(b) and (c)). Most of the variance of the underside morphology is contained in a wavenumber band between 0.001 and 0.01m⁻¹ (100-1000m). Spectral levels ranged from 1.2 to 4.2 x 10⁴ m². There is no distinct, preferred wavelength.

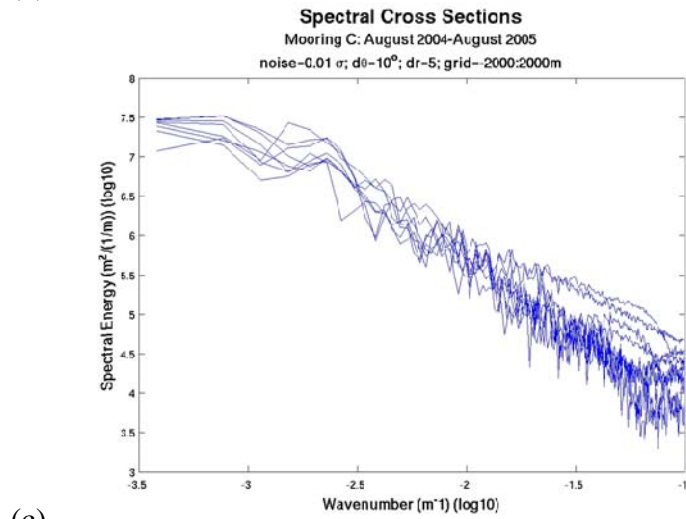
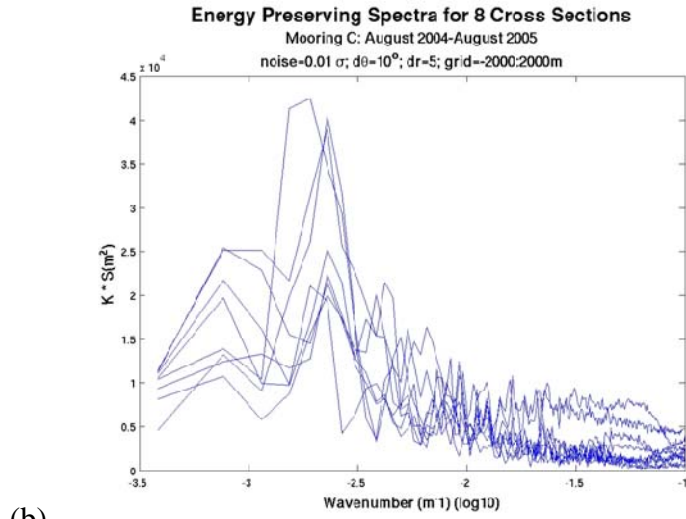
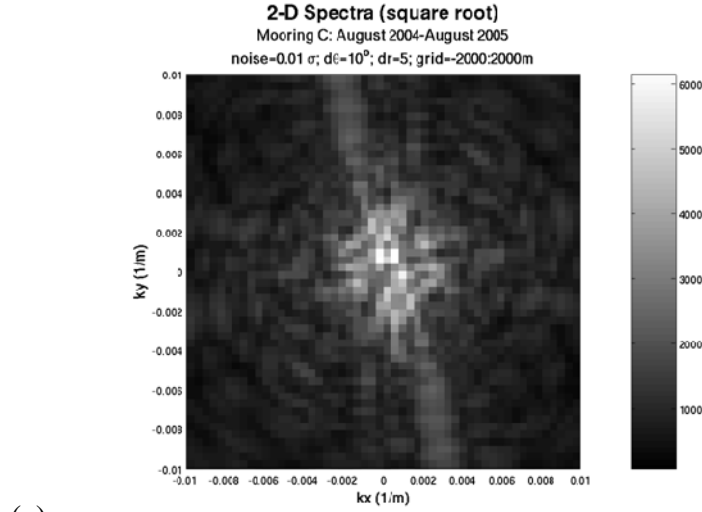


Figure 23. Mooring C: 2004-2005. (a) 2D spectrum. (b) 8 energy conserving spectral cross sections (000 to 157.5° each 22.5°). (c) 8 spectral cross sections.

In order to determine whether or not the cross sections are statistically different from one another, the standard deviation needed to be determined. This allowed confidence limits to be plotted against one another to check for overlapping regions, which would mean that there is not a difference. However, if the regions bounded by the confidence intervals were mutually exclusive, they are different and indicate anisotropy.

Determination of the confidence intervals was not straightforward. Since the data was taken at one frequency, autocorrelated, subsampled, binned, meaned and gridded in autocorrelation space before passing through a 2D FFT, degrees of freedom are impossible to determine analytically. Therefore, the degrees of freedom were determined empirically by Monte Carlo simulation. A field was created which would ultimately approximate the characteristics of the observations. This was done by starting with a field of random numbers, taking the 2D FFT, multiplying by $1/k$ and then taking the inverse 2D FFT, to get back to a Cartesian field. This new field had the properties that when it was put through the process it yielded a 2D spectrum which was comparably red like the real data, but composed of random numbers.

This random field was sampled using real buoy motion and put through the processing routine. A radial cross section was taken through the resulting spectrum. This entire process, from creating the random field through taking the cross section was repeated 30 times. For each wavenumber bin, the standard deviation of the cross sections was determined. A line was fit to approximate the standard deviation as a function of wavenumber. This represented the sigma value used for confidence limits.

Two cross sections were taken in directions which appeared to be similar (Fig. 24(a)). Even at 1 sigma, the spectra showed no regions of mutual exclusivity (Fig. 24(b)). This suggested isotropy. At 2 sigma, the confidence intervals are even wider and the overlap even greater (Fig. 24(c)). The result was to conclude that the spectrum is isotropic in these two directions.

Next, 2 cross sections were taken in directions which appeared to be significantly different (Fig. 25(a)). At 1 sigma, the spectra did show regions of mutual exclusivity, especially at the high wavenumbers, suggesting anisotropy (Fig. 25(b)). However, these

regions of exclusivity disappeared at all except for a few points when the confidence intervals were set to 2 sigma, which suggests isotropy (Fig. 25(c)). The result was to conclude that there is ‘weak’ anisotropy in this spectrum. This is defined to mean that the results were isotropic except for low levels of statistical confidence.

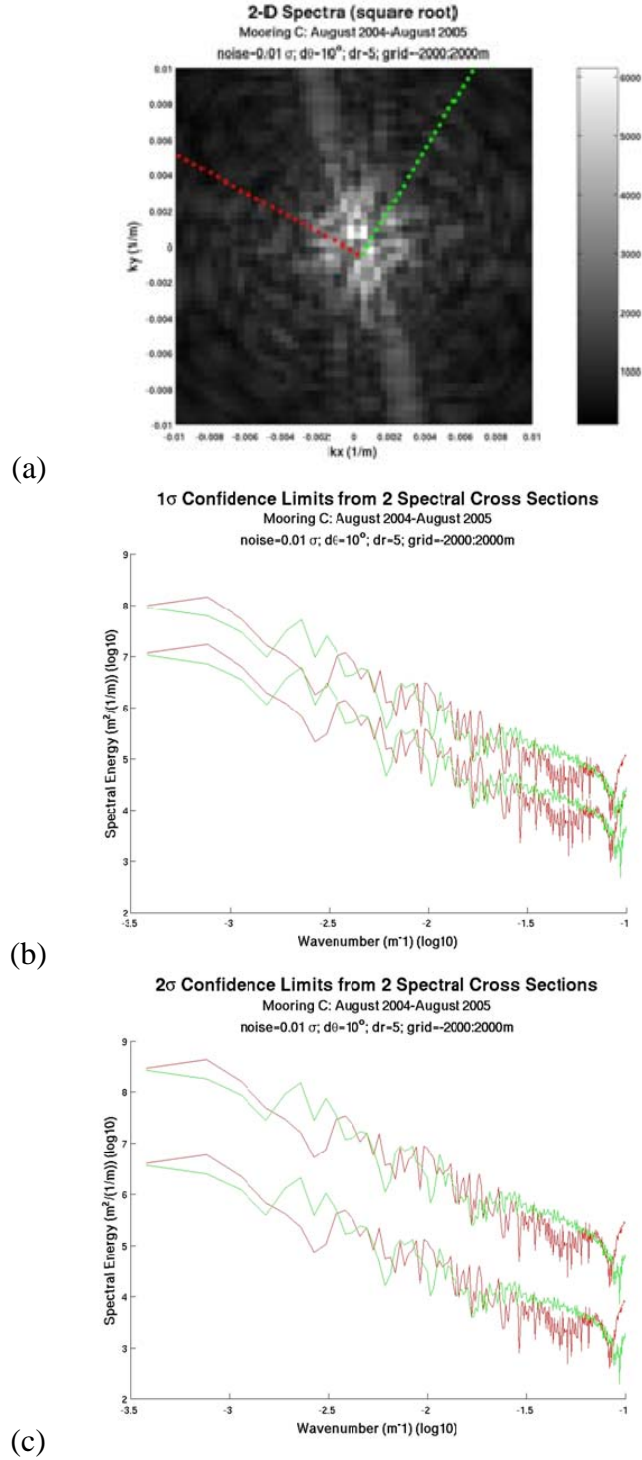


Figure 24. (a) 2 radial slices through 2D spectrum. (b) 1 sigma confidence intervals for each slice. The red lines represent the + and - 1 sigma confidence intervals for the spectral slice taken along the red dotted line in (a) and the green lines are the confidence intervals for the slice taken along the green dotted line. (c) 2 sigma confidence intervals.

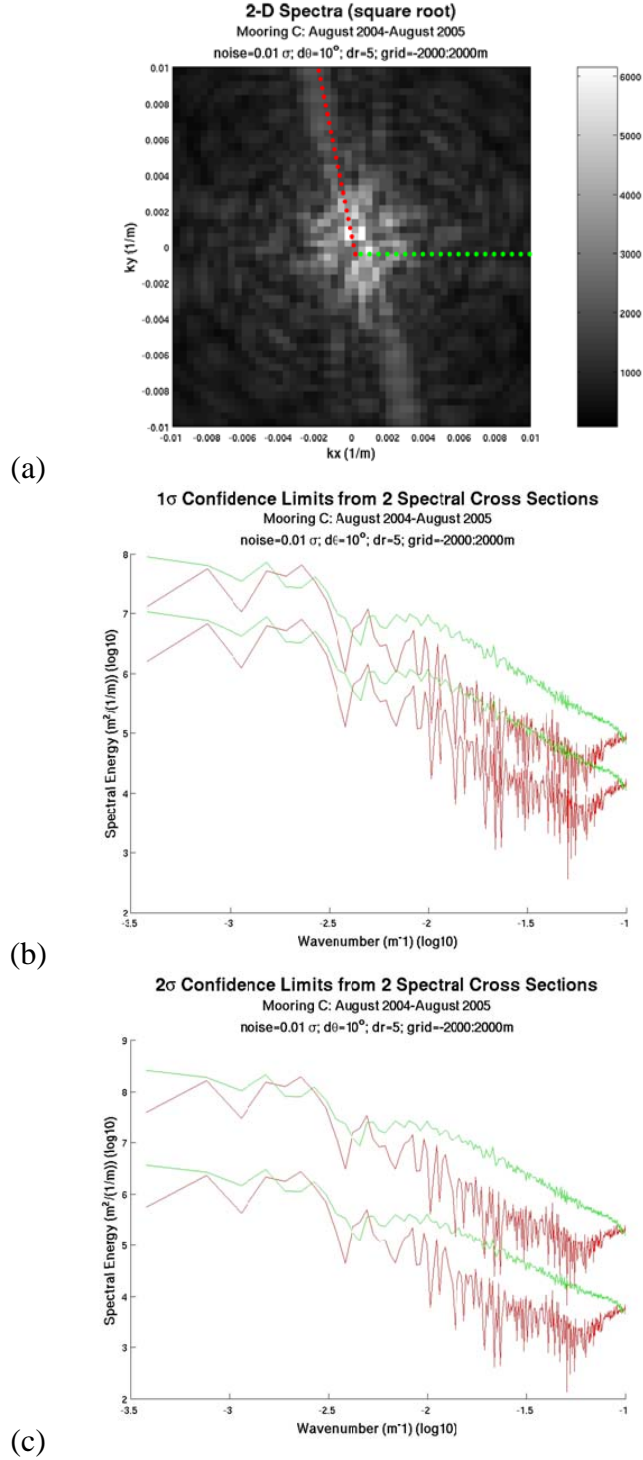


Figure 25. (a) 2 radial slices through 2D spectrum. (b) 1 sigma confidence limits for each slice. The red lines represent the + and - 1 sigma confidence intervals for the spectral slice taken along the red dotted line in (a) and the green lines are the confidence intervals for the slice taken along the green dotted line. (c) 2 sigma confidence intervals.

To ensure that the observed anisotropy was not a function of the binning process, a “red” field like the one used to generate the confidence intervals was sent through the process. Cross sections were taken in the 2 directions which showed the greatest amounts of anisotropy for the previous run. The result showed that the spectrum was isotropic, even at one sigma (Fig. 26). This shows that the observed isotropy was a characteristic of the real data and not the processing routine.

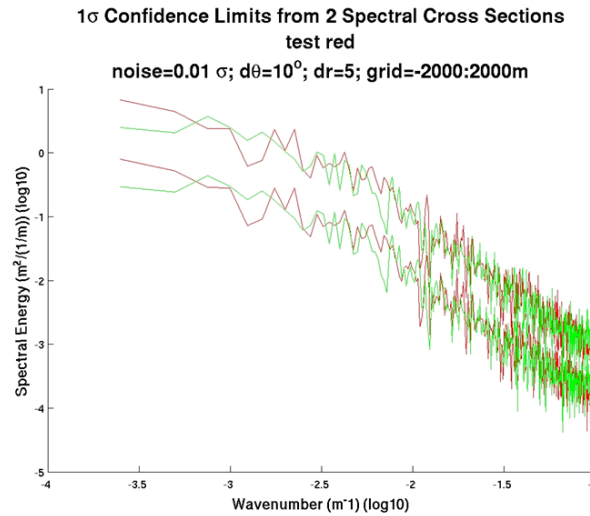


Figure 26. 1 sigma confidence intervals from the spectral cross sections from the synthetic “red” field taken in the same directions as Fig. 25.

2. Summary for Other Data Sets

There were directional differences observed in the spectra of all data sets at 1 sigma. These suggest anisotropy. However, this was never true at 2 sigma, where the spectra appeared isotropic. Furthermore, although the isotropic regions observed usually occurred at high wavenumbers, they were also sometimes observed throughout the rest of the spectra. As for the data from Mooring C from 2004-2005, most of the variance of the other datasets is contained in a wavenumber band between 0.001 and 0.01m^{-1} (100 - 1000m). Again, there are no distinct, preferred wavelengths. Spectral levels ranged from $0.2 - 1.6 \times 10^4 \text{ m}^2$ for Mooring A from 2004-2005 to $0.3 - 3.3 \times 10^4 \text{ m}^2$ for Mooring C from 2003-2004.

In summary, the spectra are weakly anisotropic for the wavenumbers resolved in this study.

C. SPATIAL AND TEMPORAL COMPARISONS

The weak anisotropy observed was not consistent from one mooring to another. The 2D spectra are displayed in Figs. 27 and 28. Spatial and temporal comparisons failed to determine a consistent directional preference. However, most of the variance was contained in the $.001$ to $.01\text{m}^{-1}$ wavenumber band (100-1000m) for all datasets. Spectral levels varied significantly between the datasets.

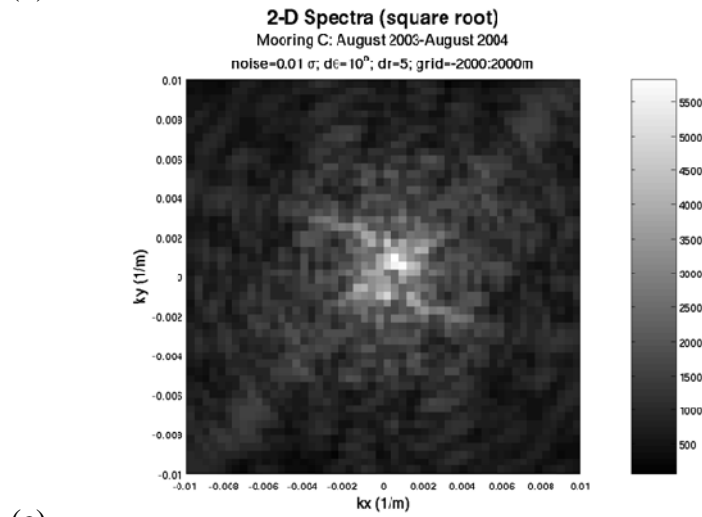
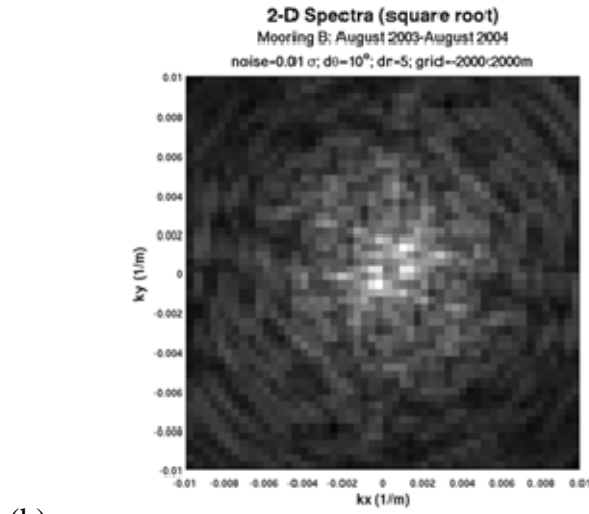
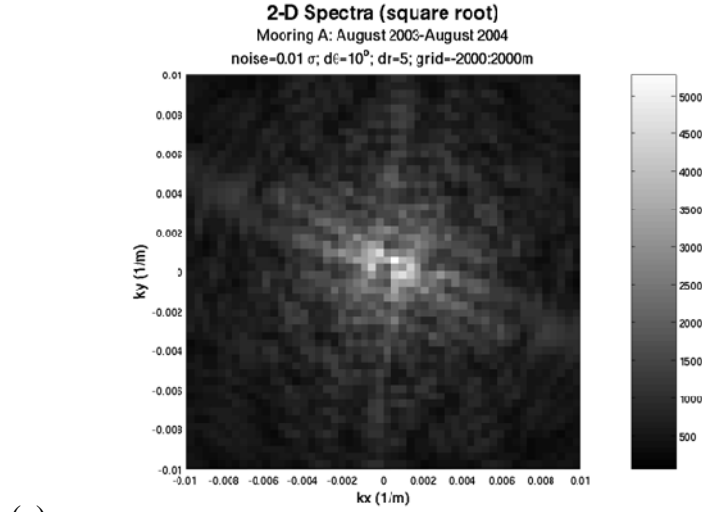
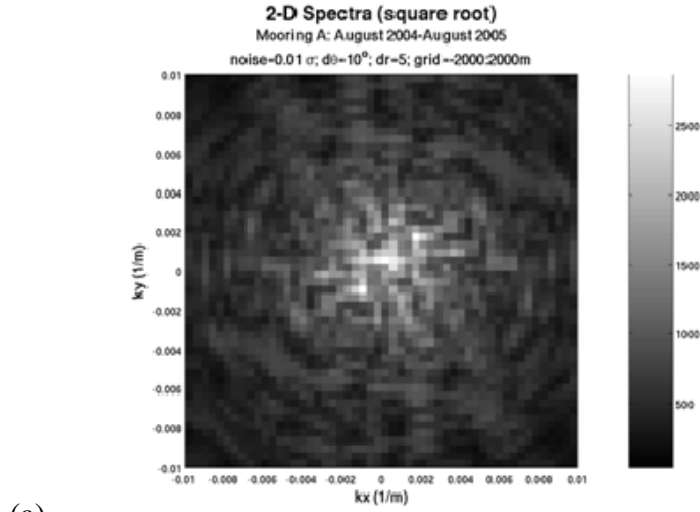
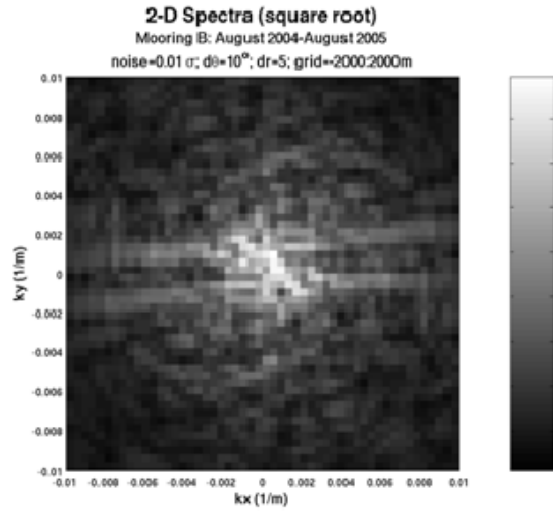


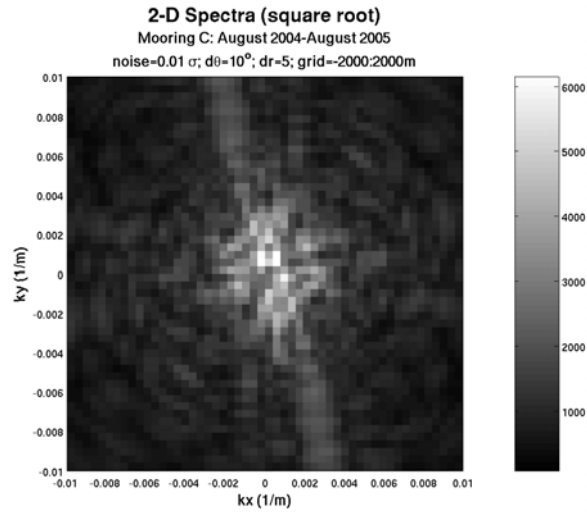
Figure 27. 2D spectra of under ice roughness from August 2003-August 2004. (a) Mooring A. (b) Mooring B. (c) Mooring C.



(a)



(b)



(c)

Figure 28. 2D spectra of under ice roughness from August 2004-August 2005. (a) Mooring A. (b) Mooring B. (c) Mooring C.

D. COMPARISONS TO OTHER RESEARCHERS

This weak anisotropy does not agree with the findings of Davis and Wadhams (1995). While working from a submarine, they gathered concurrent upward looking echosounder and towed sidescan sonar which allowed for determination of both ice draft and ice keel orientation. Their findings showed that there was anisotropy in the alignment of the large ice roughness elements, the ice keels. Their data showed lineation which fell roughly into two preferred alignments. When considered in the context of the area in which the data were gathered, the directions are roughly along and perpendicular to the Greenland coast (Fig. 29). The observed ice keels could be the result of ridging due to compression caused by downstream boundary and shearing caused by motion of Transpolar Drift Stream.



Figure 29. Ridge orientation vectors (Davis and Wadhams, 1995).

Comparisons to the findings of Davis and Wadhams and this project should be made carefully. This project used data from the Beaufort Gyre, well away from land boundaries. Furthermore, the data was collected from moorings in deep water (greater than 3500m) so there was no bottom interaction or grounding to cause a preferred angle of orientation for roughness elements.

Hibler (1972) first suggested the process upon which this project was based. Using his version of data processing, he found anisotropy to suggest a preferred lineation of pressure ridge sails in the Beaufort. However, this was based on one case using three intersecting laser profiles about 2400m long collected by aircraft. In contrast, this project used several hundred profiles in three locations in the Beaufort over the course of two years. Again, comparisons must be made carefully.

E. TURBULENCE IMPLICATIONS

The implications of the weak anisotropy that was observed is that directionality is important at very small scales. In turbulence simulations, where roughness is significant, a ‘spectral’ approach is most appropriate to approximate a near-isotropic field. In contrast, most conceptual models of flow over roughness have been developed with regular arrays of ridges and keels with a single orientation and fixed spacing (Arya, 1975).

Density profiles obtained at APLIS-2007 in the Beaufort Sea showed pycnoclines which were significantly shallower than those historically observed (Fig. 30). This shoaling of the thermocline is possibly explained by the recent accelerating rate of ice melt. Pycnoclines at shallow depths can produce the “dead water” effect if an ice keel is dragged through them. With any anisotropy in the ice roughness, especially for deep ice keels whose depth is comparable to or exceeding the pycnocline depth, there will be significant effects on the momentum budget. Energy will be lost at variable rates depending on the direction that the ice flow is drifting.

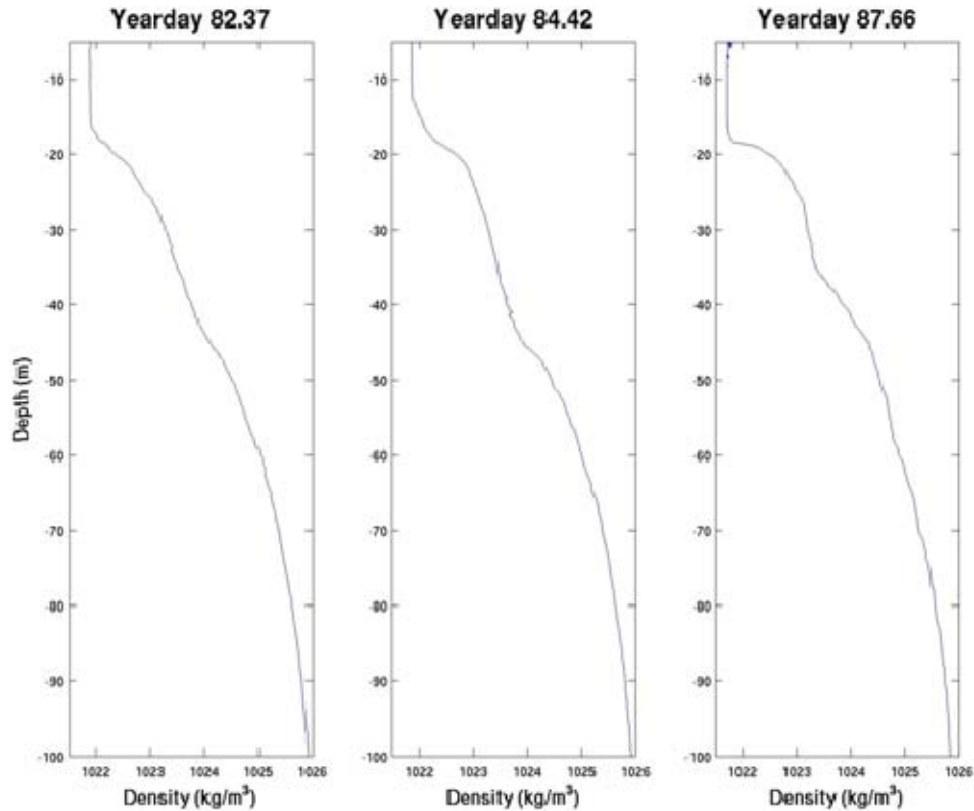


Figure 30. Density profiles from APLIS 2007. Note the shallow pycnocline; historically the pycnocline has been observed near 35m.

F. POSSIBLE MITIGATING EFFECT

An observation made recently showed that the ice floe used for APLIS-2007 rotated significantly, changing heading by 11 degrees in 7 days (Fig. 31) (Hutchings, 2007). This has the potential to mitigate the effects of weak directional dependence that were observed in this study, making the time averaged roughness isotropic. The APLIS-2007 observation is considered abnormal when compared to previous ice camp rotation measurements. However, as the Arctic pack ice becomes thinner and more mobile, more rotation is possible. This would make conditions more isotropic, and should be investigated further to determine if it is a new trend.

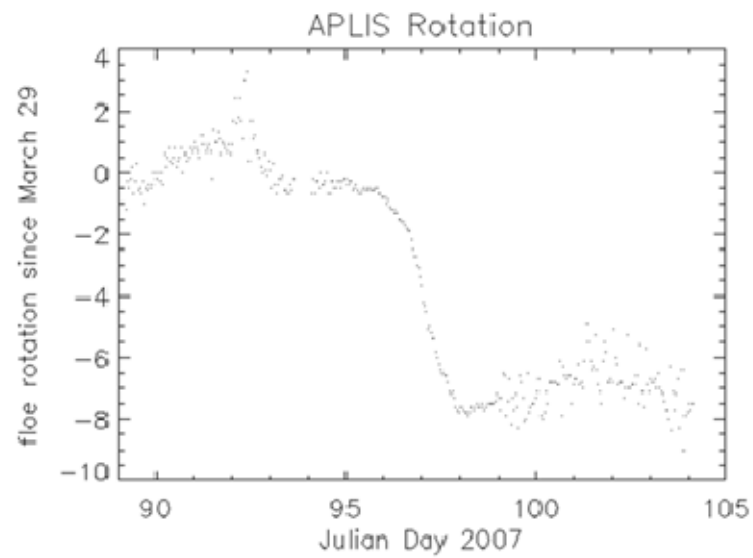


Figure 31. Plot of APLIS 2007 ice floe rotation (Hutchings, 2007).

V. CONCLUSIONS

The roughness of the ice underside plays a role in turbulent ocean heat, salt and momentum fluxes that determine the delicate balance between surface forcing and the ocean interior that sustains or reduces the perennial ice cover. It has climate, engineering, and naval implications as well.

This project took sparsely sampled ice draft data and processed it in such a way that the 2D wavenumbers were conserved in order to produce a realistic 2D spectrum of under-ice roughness. The process was validated using several test cases. It showed weak anisotropy of under-ice roughness at scales between 10m and 2000m for pack ice in the Beaufort Gyre. Error estimates were determined by Monte Carlo simulations. For each dataset, most of the variance of the underside morphology was contained in a wavenumber band between 0.001 and 0.01m^{-1} (100-1000m). There were no distinct, preferred wavelengths. Spectral levels ranged from $1.2 - 4.2 \times 10^4 \text{ m}^2$ for Mooring C (2004-2005) to $0.2 - 1.6 \times 10^4 \text{ m}^2$ for Mooring A (2004-2005).

Future studies will benefit from the new mooring configurations in the Beaufort Gyre Exploration Project. The new moorings have colocated ULS and ADCPs which when set in bottom tracking mode give the true local ice motion at the mooring. There no longer needs to be interpolation between buoys or assumptions of continuous ice motion. This increased amount of data will allow tighter limits in the processing routine and ultimately a higher resolution 2D roughness spectrum.

THIS PAGE INTENTIONALLY LEFT BLANK

LIST OF REFERENCES

- Arya, S. P. S. (1975). A drag partition theory for determining the large-scale roughness parameter and wind stress on the arctic pack ice, *J. Geophys. Res.*, 80, 3447-3454.
- BBC News (2005). Norway fish officials handed over. *BBC News* [online], <http://news.bbc.co.uk/2/hi/europe/4359574.stm>, accessed 10 Feb 2008.
- CBC News (2007). Ottawa buying up to 8 Arctic patrol ships. *CBC News* [online], <http://www.cbc.ca/canada/story/2007/07/09/arctic-cda.html>, accessed 11 Feb 2008.
- Bourke, R.H. and A.S. McLaren (1992). Contour mapping of Arctic Basin ice draft and roughness parameters. *J. Geophys. Res.*, 97(C11), 17715-17728.
- Damron, D. (1997). Fish settle border dispute. *Arctic Science Journeys* [online], http://seagrant.uaf.edu/news/97ASJ/04.29.97_BorderDispute.html, accessed 28 Feb 2008.
- Davis, N.R. and P. Wadhams (1995). A statistical analysis of Arctic pressure ridge morphology. *J. Geophys. Res.*, 100(C6), 10915-10925.
- Elliott, S. M. (2007). *USCGC Healy (WAGB 20) Press Release of 30 Sep 2007* [online], http://www.uscg.mil/pacarea/healy/deployments/AWS07/XO/Press%20Releases/Sept_30_2007_release.htm, accessed 10 Feb 2008.
- Fowler, C. (2003, updated 2007). *Polar Pathfinder Daily 25 km EASE-Grid Sea Ice Motion Vectors*. Boulder, Colorado USA: National Snow and Ice Data Center. Digital media.
- Hibler, W.D. III (1972). Two dimensional statistical analysis of Arctic sea ice ridges. In *Sea Ice* (ed. T. Karlsson), Nat. Res. Counc. of Iceland, Reykjavik, 261-275.
- Hutchings, J. (2007). *APLIS 07* [online], http://aplis07.iarc.uaf.edu/index.php/Public_Data, accessed 10 Feb 2008.
- Krishfield, R. and A. Proshutinsky (2006). BGOS ULS Processing Procedure. *Woods Hole Oceanographic Institution* [online], <http://www.whoi.edu/beaufortgyre/pdfs/BGOS%20ULS%20Data%20Processing%20Procedure.pdf>, accessed 10 Feb 2008.
- Kutschale, H. (1969). Arctic hydroacoustics. *Arctic*, 22(3), 246-264.

- Melling, H. and D.A. Riedel (1995). The underside topography of sea ice over the continental shelf of the Beaufort Sea in the winter of 1990. *J. Geophys. Res.*, 100(C7), 13641-13653.
- Melling, H., P.H. Johnston and D.A. Riedel (1995). Measurements of the Underside Topography of Sea Ice by Moored Subsea Sonar. *J. Atmos. Oceanic Technol.*, 12, 589-602.
- National Science Foundation (1998). Newly Declassified Submarine Data Will Help Study of Arctic Ice. *NSF Press Release 98-006* [online], http://www.nsf.gov/news/news_summ.jsp?cntn_id=102863, accessed 10 Feb 2008.
- National Snow and Ice Data Center. (1998, updated 2006). *Submarine upward looking sonar ice draft profile data and statistics*. Boulder, Colorado USA: National Snow and Ice Data Center/World Data Center for Glaciology. Digital media.
- Nicholson, J.H. (2008). Through the Bering Strait in Mid-Winter. *USS SARGO (SSN 583)* [online], <http://www.ssn583.com/History/NicholsonReview.htm>, accessed 05 FEB2008.
- Proshutinsky, A. (2008). Beaufort Gyre Exploration Project- Mooring Data. *Woods Hole Oceanographic Institution* [online], http://www.whoi.edu/beaufortgyre/data_moorings.html, accessed 10 Feb 2008.
- Reid, T. (2007). Arctic military bases signal new cold war. *The Times Online* [online], http://www.timesonline.co.uk/tol/news/world/us_and_americas/article2238243.ece, accessed 10 Feb 2008.
- Rigor, I. (2002). *IABP drifting buoy, pressure, temperature, position, and interpolated ice velocity*. Compiled by the Polar Science Center, Applied Physics Laboratory, University of Washington, Seattle, in association with NSIDC. Boulder, CO: National Snow and Ice Data Center. Digital media.
- Shukman, D. (2007). Ice melt raises passage tension. *BBC News* [online], <http://news.bbc.co.uk/2/hi/science/nature/7033498.stm>, accessed 07 Feb 2008.
- Skillingstad, E. D., C. A. Paulson, W. S. Pegau, M. G. McPhee and T. Stanton (2003). Effects of keels on ice bottom turbulence exchange. *J. Geophys. Res.*, 108, 3372-3386.
- Wadhams, P. (1978). Characteristics of deep pressure ridges in the Arctic Ocean. *POAC 77*, Proceedings of the Fourth International Conference on Port and Ocean Engineering under Arctic Conditions, St. John's, I, 544-555. Memorial Univ., St. John's., Nfld.

Wadhams, P. (2002). *Ice in the Ocean*. Gordon and Breach Science Publishers, London, 351pp.

Wadhams, P. and T. Davy (1986). On the spacing and draft distributions for pressure ridge keels. *J. Geophys. Res.*, 91(C9), 10697-10708.

WCRP Informal Report No. 15/2004: Workshop on Sea-Ice Thickness Measurements from Moored Ice-Profiling Sonars: Calibration, Data Processing and Application (Tromsø, Norway, 1-3 July 2002).

THIS PAGE INTENTIONALLY LEFT BLANK

INITIAL DISTRIBUTION LIST

1. Defense Technical Information Center
Ft. Belvoir, Virginia
2. Dudley Knox Library
Naval Postgraduate School
Monterey, California